Local palmitoylation cycles define activity-regulated postsynaptic subdomains

Yuko Fukata,[1] Ariane Dimitrov,[2,3] Gaelle Boncompain,[2,3] Ole Vielemeyer,[2,3] Franck Perez,[2,3] and Masaki Fukata[1]

[1]Division of Membrane Physiology, Department of Cell Physiology, National Institute for Physiological Sciences, Okazaki, Aichi 444-8787, Japan
[2]Centre National de la Recherche Scientifique, Unité Mixte de Recherche 144 and [3]Institut Curie Centre de Recherche, 75248 Paris Cedex 05, France

Distinct PSD-95 clusters are primary landmarks of postsynaptic densities (PSDs), which are specialized membrane regions for synapses. However, the mechanism that defines the locations of PSD-95 clusters and whether or how they are reorganized inside individual dendritic spines remains controversial. Because palmitoylation regulates PSD-95 membrane targeting, we combined a conformation-specific recombinant antibody against palmitoylated PSD-95 with live-cell super-resolution imaging and discovered subsynaptic nanodomains composed of palmitoylated PSD-95 that serve as elementary units of the PSD. PSD-95 in nanodomains underwent continuous de/repalmitoylation cycles driven by local palmitoylating activity, ensuring the maintenance of compartmentalized PSD-95 clusters within individual spines. Plasma membrane targeting of DHHC2 palmitoyltransferase rapidly recruited PSD-95 to the plasma membrane and proved essential for postsynaptic nanodomain formation. Furthermore, changes in synaptic activity rapidly reorganized PSD-95 nano-architecture through plasma membrane–inserted DHHC2. Thus, the first genetically encoded antibody sensitive to palmitoylation reveals an instructive role of local palmitoylation machinery in creating activity-responsive PSD-95 nanodomains, contributing to the PSD (re)organization.

Introduction

Organization of specialized membrane domains, such as focal adhesions, tight junctions, and pre/post-synapses, requires ordered protein assembly at the plasma membrane. In neurons, proteins that mediate synaptic vesicle fusion and neurotransmitter release concentrate specifically at the presynaptic active zone. Correspondingly, neurotransmitter receptors, postsynaptic scaffolding proteins, and various signaling proteins precisely align at a specialized postsynaptic membrane region, called the postsynaptic density (PSD). The size, shape, and protein composition of the PSD determine the function of individual excitatory synapses.

PSD-95 is the most abundant scaffold protein specifically enriched in the PSD. It contains three PDZ domains, an SH3 domain, and a guanylate kinase (GuK)–like domain (Kim and Sheng, 2004; Funke et al., 2005). Through its PDZ domains, PSD-95 assembles at the PSD various synaptic components including intracellular signaling molecules (e.g., SynGAP and kalirin-7), ion channels (e.g., stargazin/AMPA receptors [AMPARs] and NMDA receptors), and cell adhesion molecules (e.g., neuroligin). The following observations indicate that PSD-95 plays a primary role in synaptic development and maturation: (1) PSD-95 clusters at synapses before other postsynaptic proteins (Rao et al., 1998) and lies closer to the postsynaptic membranes than other proteins (Valtschanoff and Weinberg, 2001; Dani et al., 2010); (2) reduced expression of PSD-95 causes patchy loss of the PSD area (Chen et al., 2011); and (3) overexpression of PSD-95 can drive maturation of glutamatergic synapses (El-Husseini et al., 2000b). In addition, PSD-95 regulates synaptic transmission and plasticity by regulating the molecular composition of the PSD, including

F. Perez and M. Fukata contributed equally to this paper.

Correspondence to Masaki Fukata: mfukata@nips.ac.jp; or Franck Perez: Franck.Perez@curie.fr

O. Vielemeyer's present address is Drexel University College of Medicine, Philadelphia, PA.

Abbreviations used in this paper: 2-BP, 2-bromopalmitate; AMPAR, α-amino-3-hydroxy-5-methyl-4-isoxazole propionic acid receptor; CS, cysteine-to-serine mutation; DHHC, aspartate-histidine-histidine-cysteine; DIV, days in vitro; FWHM, full width at half maximum; GuK, guanylate kinase; PAT, palmitoyl acyltransferase; PSD, postsynaptic density; PSTCD, *Propionibacterium shermanii* transcarboxylase domain; RUSH, retention using selective hooks; scFv, single-chain variable fragment; shRNA, short hairpin RNA; STED, stimulated emission depletion; TARP, transmembrane AMPAR regulatory protein; TEV, tobacco etch virus; TTX, tetrodotoxin; WT, wild type.

The Rockefeller University Press $30.00
J. Cell Biol. Vol. 202 No. 1 145–161
www.jcb.org/cgi/doi/10.1083/jcb.201302071

the number of synaptic AMPARs (El-Husseini et al., 2000b; Béïque et al., 2006; Ehrlich et al., 2007; Elias and Nicoll, 2007). Protein–protein interactions and palmitoyl lipid modification each play important roles in the postsynaptic targeting of PSD-95 (Craven et al., 1999). The neurexin–neuroligin trans-synaptic interaction triggers PSD-95 recruitment through a PDZ-domain–mediated interaction (Graf et al., 2004; Chih et al., 2005; Nam and Chen, 2005). However, neurons derived from neuroligin triple knockout mice still show normal synaptic accumulation of PSD-95 (Varoqueaux et al., 2006). Palmitoylation of PSD-95 at its N-terminal cysteine residues is essential for its postsynaptic targeting, as a palmitoylation-deficient PSD-95 mutant is diffusely distributed in dendrites and the cell body (Topinka and Bredt, 1998). It remains still unclear, however, what defines the location of PSD-95 clusters, and how PSD-95 clusters are maintained and remodeled to regulate the organization of the entire PSD.

Protein palmitoylation is a frequent lipid modification that regulates protein trafficking to intracellular or plasma membranes (El-Husseini Ael and Bredt, 2002; Resh, 2006; Linder and Deschenes, 2007; Fukata and Fukata, 2010; Salaun et al., 2010; Sen and Snyder, 2010). This modification is reversibly catalyzed by DHHC-type palmitoyl acyltransferases (PATs) and still uncharacterized depalmitoylating enzymes. Recent live-cell imaging experiments using fluorescently tagged palmitoyl substrates (e.g., H-Ras, Gα, and PSD-95) and a palmitoylation inhibitor revealed a role for palmitoylation in the dynamic relocalization of palmitoyl proteins between membrane compartments (Rocks et al., 2005; Chisari et al., 2007; Noritake et al., 2009; Tsutsumi et al., 2009). However, exogenously expressed fluorescent proteins may not necessarily behave like their endogenous counterparts and the use of overexpressed proteins may cause more subtle physiological properties to be overlooked.

Here, we developed a novel probe for spatiotemporally visualizing the palmitoylation state of endogenous PSD-95. This probe revealed an important role of local palmitoylation cycles to functionally organize activity-responsive nanodomains of PSD-95 in the postsynapse.

Results

Selection of a palmitoylation-specific recombinant antibody against PSD-95, PF11

To visualize the palmitoylation state of endogenous PSD-95 in fixed and in living cells, we generated a palmitoylation-specific biosensor. We took advantage of the antibody phage display system, which has allowed selection of powerful conformation-specific recombinant antibodies (Nizak et al., 2003b; Dimitrov et al., 2008). We screened a phage display library of recombinant single-chain variable fragment (scFv) antibodies against palmitoylated PSD-95. The antigen was purified from HEK293T cells coexpressing PSD-95-GFP fused to PSTCD, a biotin acceptor peptide, and one of PSD-95 PATs, DHHC15 (with DHHC2, 3, and 7; Fig. 1, A–C; Fukata et al., 2004). The subsequent antibody selection screen yielded a promising scFv clone, named PF11 (Fig. 1 C). In fixed hippocampal neurons, hPF11 (PF11 fused to human IgG Fc) specifically stained endogenous PSD-95 clusters, as indicated by the lack of staining in PSD-95 knockdown neurons (Fig. 1 D). In adult mouse brain sections, hPF11 antibody showed strong punctate signals in the neuropil of, for example, hippocampus and cerebellum, and its overall staining pattern was consistent with that of a conventional PSD-95 antibody (Fig. 1 E).

We next tested whether PF11 distinguishes palmitoylated PSD-95 from nonpalmitoylated PSD-95. When expressed with DHHC2 in HEK293T cells, wild-type PSD-95 (PSD-95 WT-GFP) was found at the plasma membrane (Fig. 1 F), where it was recognized by hPF11. In contrast, a palmitoylation-deficient PSD-95 mutant, in which the N-terminal palmitoyl cysteines 3 and 5 were mutated to serines (PSD-95 CS-GFP), was diffusely distributed in the cytoplasm and not stained with hPF11 (Fig. 1 F). PF11 specificity for palmitoylated PSD-95 was confirmed in hippocampal neurons using a molecular replacement strategy. Expression of endogenous PSD-95 was reduced via shRNA knockdown and replaced by expression of either a PSD-95 WT or PSD-95 CS; both constructs were shRNA resistant (Fig. 1 G). PSD-95 WT was localized as clusters at dendritic spines and clearly labeled by hPF11. In contrast, PSD-95 CS was diffusely distributed in the cell body and dendrites and was not recognized by hPF11. Thus, PF11 recognition of PSD-95 expressed in cells depends on PSD-95 palmitoylation.

We compared signals of hPF11 (representing palmitoylated PSD-95) with those of a conventional PSD-95 antibody (representing total PSD-95) in neurons. hPF11 signals were specifically detected as small discrete puncta in dendrites and hardly detected in the soma (Fig. 2, A and B). Nearly all dendritic hPF11 signals overlapped with or were closely apposed to a presynaptic marker protein, vGlut1 (Fig. 2 B, shown by asterisks). In contrast, total PSD-95 signals were occasionally present outside synaptic sites in both dendrites and the soma (Fig. 2, A and B, with neither vGlut1 nor hPF11 signals shown by arrows). When virtually all the hippocampal glutamatergic excitatory synapses were labeled with the mixture of two antibodies against vGlut1 and vGlut2 (vGlut), 97.4 ± 1.2% of hPF11 and 89.9 ± 1.5% of total PSD-95 signals were colocalized or closely apposed with vGlut signals in dendritic regions ($P < 0.001$, Student's t test; five neurons, ∼2,000 clusters), indicating that hPF11 antibody exclusively labels postsynaptic PSD-95 clusters. We observed a higher intensity ratio of dendritic spines vs. soma fluorescence when staining neurons with hPF11 (ratio, 19.5 ± 4.5) than when staining total PSD-95 (ratio, 6.7 ± 1.9; $P < 0.001$, Student's t test; 6 neurons). Upon treatment with 2-bromopalmitate (2-BP), which inhibits protein palmitoylation, hPF11 signals at the spines were reduced sensitively, but signals in the soma were not reduced (Fig. 2, C and D). These results directly demonstrate for the first time that palmitoylated PSD-95 is almost exclusively localized at excitatory synapses in neurons and that depalmitoylation of PSD-95 specifically occurs at the synapse.

PF11 as an intrabody tracks palmitoylated PSD-95 conformation in living cells

Next, we examined PF11's ability to recognize palmitoylated PSD-95 in living cells. PF11 cDNA was fused with GFP cDNA and used as a fluorescent intracellular antibody (Fig. 1 C), as described previously (Nizak et al., 2003b). This intrabody was coexpressed with PSD-95-mCherry in HEK293T cells (Fig. 3, A–F).

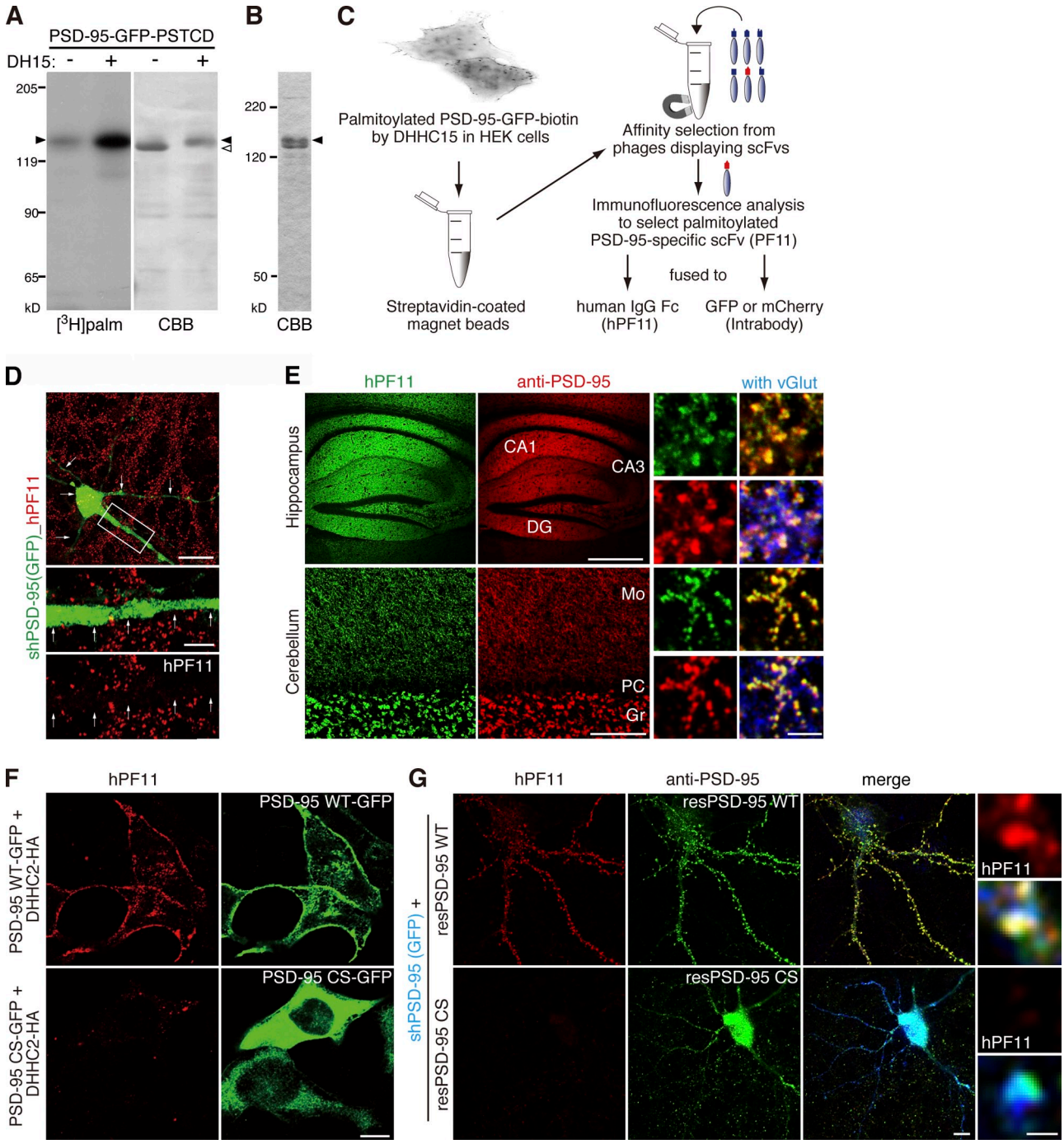

Figure 1. **Selection of PF11, a recombinant antibody specific for palmitoylated PSD-95.** (A) PSD-95-GFP-PSTCD metabolically labeled with [^{3}H]palmitic acid in HEK293T cells was analyzed by fluorography ([^{3}H]palm) and Coomassie brilliant blue (CBB) staining. Closed and open arrowheads indicate the positions of palmitoylated and nonpalmitoylated PSD-95, respectively. (B) Palmitoylated PSD-95-GFP-PSTCD was purified to near homogeneity. (C) A combinatorial recombinant antibody library was screened in vitro against palmitoylated PSD-95. A promising clone, PF11, was obtained. (D) Indirect PF11 immunofluorescence. The signal (hPF11, red) disappeared in PSD-95 knockdown neurons (shPSD-95, green, arrows). Bars, 20 µm (5 µm, magnified). (E) hPF11 (green) and PSD-95 (red) antibodies showed the similar staining pattern in the hippocampus (top) and cerebellum (bottom) of adult mouse brain sections. Glutamatergic presynapses were labeled with the mixture of vGlut1 and vGlut2 antibodies (blue). DG, dentate gyrus; Mo, molecular layer; PC, Purkinje cell layer; Gr, granule cell layer. Regions in the molecular layer of DG and cerebellum are magnified (right panels). Bars: (top) 500 µm; (bottom left) 100 µm; (bottom right) 2.5 µm. (F) HEK293T cells were cotransfected with DHHC2 and either PSD-95 wild-type (WT) or cysteine-mutated palmitoylation-deficient PSD-95 CS, and cells were stained with hPF11 (red). Bar, 10 µm. (G) hPF11 staining (red) was detected in neurons expressing shPSD-95 (marked by GFP, blue pseudocolor) and complemented by shRNA-resistant (res) PSD-95 WT (stained by anti-PSD-95, green pseudocolor), but not by palmitoylation-deficient resPSD-95 CS. Bars, 10 µm (1 µm, dendritic spines magnified).

Under control conditions, PF11-GFP was diffusely dispersed throughout the cell (Fig. 3 A). In the presence of DHHC2, PF11-GFP and PSD-95-mCherry cotranslocated to the plasma membrane or occasionally to vesicular transport intermediates (Fig. 3, B and C). An intrabody against a nonrelated protein, CC7-GFP, remained dispersed throughout the cell when expressed

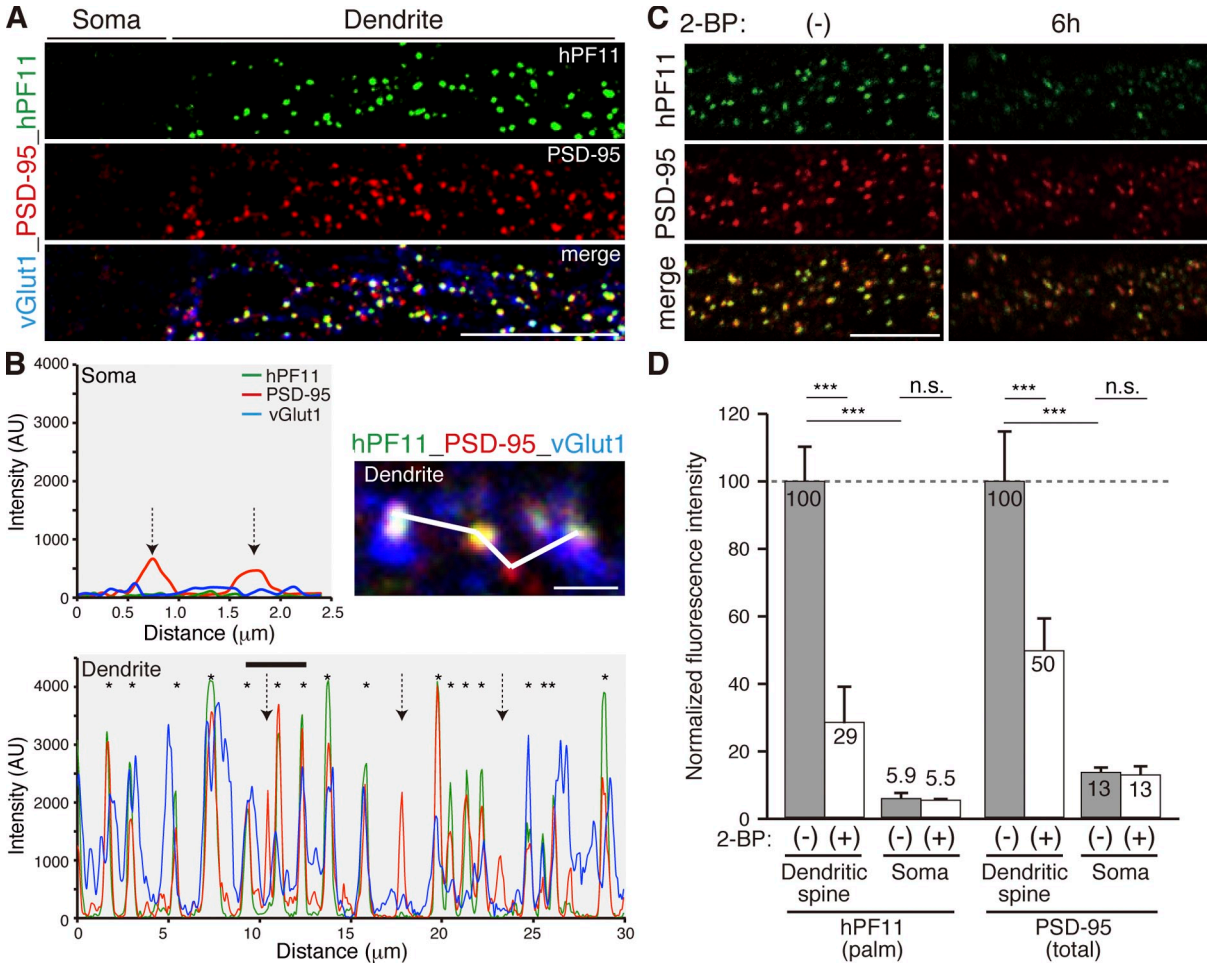

Figure 2. **PF11 distinguishes postsynaptic PSD-95 from extrasynaptic PSD-95.** (A and B) Hippocampal neurons were stained triply with hPF11, PSD-95, and vGlut1 antibodies. Asterisks in intensity profiles (B) indicate postsynaptic hPF11 signals (green) colocalized with total PSD-95 (red) and vGlut1 staining (blue), and arrows indicate extrasynaptic PSD-95 signals devoid of hPF11 and vGlut1 signals. A dendritic region indicated by a thick black bar in the intensity profile is magnified (B). Representative profiles from ten repeats (three neurons) are shown (B). (C and D) Hippocampal neurons were treated with or without 2-bromopalmitate (2-BP; 100 µM, 6 h) and stained with hPF11 and PSD-95 antibodies. Representative dendritic regions are shown (C). 300–400 dendritic clusters and 30–40 soma clusters from 5 neurons were analyzed for fluorescence intensities of green and red channels (D). palm, palmitoylated PSD-95. n.s., not significant; ***, $P < 0.001$, determined by one-way ANOVA with post-hoc Tukey's test. Bars: (A) 10 µm; (B) 1 µm; (C) 5 µm.

with palmitoylated PSD-95 (not depicted). When DHHC2 palmitoylating activity was blocked with 2-BP, PSD-95-mCherry detached from the plasma membrane. PF11-GFP was similarly released in the cytoplasm, dissociating from the plasma membrane and from intracellular aggregates of PSD-95-mCherry (Fig. 3, D and F). Specific binding of PF11-GFP to palmitoylated PSD-95 was also observed in immunoprecipitation experiments. More PSD-95-mCherry was coimmunoprecipitated with PF11-GFP when cells overexpressed DHHC2, whereas the binding was prevented in cells pretreated with 2-BP (Fig. 3 E). Binding of PF11-GFP to PSD-95 CS did not occur. Thus, PF11 can serve as an intrabody to track palmitoylated PSD-95 in intact cells.

We next asked whether PF11 is a palmitoylation site-specific or conformation-specific antibody. We coexpressed a series of chimeric or deleted PSD-95-GFP constructs with PF11-mCherry in HEK293T cells (Fig. 3 F and Fig. S1, A–G). A PSD-95 mutant that contained a prenylated and dually palmitoylated motif of paralemmin at the C terminus of PSD-95 CS-GFP (PSD-95 CS-GFP/Para) was localized at the plasma membrane but was not recognized by PF11-mCherry (Fig. S1 B), which indicates that PF11 binding requires N-terminal modification of PSD-95. As expected, GAP43, which is another N-terminally palmitoylated protein, was not recognized by PF11 (Fig. S1 C) and PF11 did not react with palmitoylated PSD-93, which is closely related to PSD-95 (Fig. 3 F). Importantly, PF11 recognized PSD-95 chimeric constructs in which the short N-terminal palmitoylation motif of PSD-95 had been replaced with that of GAP43 (+GAP43-N11, Fig. S1 D) or with another type of acylation motif (the N-terminal myristoylation motif of Src, +Src-N20; Fig. S1 E). Furthermore, the antibody did not react with either a short palmitoylated motif from PSD-95 (N13, 1–13 aa) or with palmitoylated 1-SH3 (1–495 aa), which lacked the GuK domain (Fig. 3 F). In contrast, PSD-95 d(PDZ1,2), which lacked the first and second PDZ domains, was detected by PF11 in a palmitoylation-dependent manner (Fig. S1, F and G). The GuK domain (533–699 aa) was necessary for the interaction of palmitoylated PSD-95 d(PDZ1,2) with PF11 (Fig. 3 F and Fig. S1 F). However, the GuK domain alone was not sufficient for binding

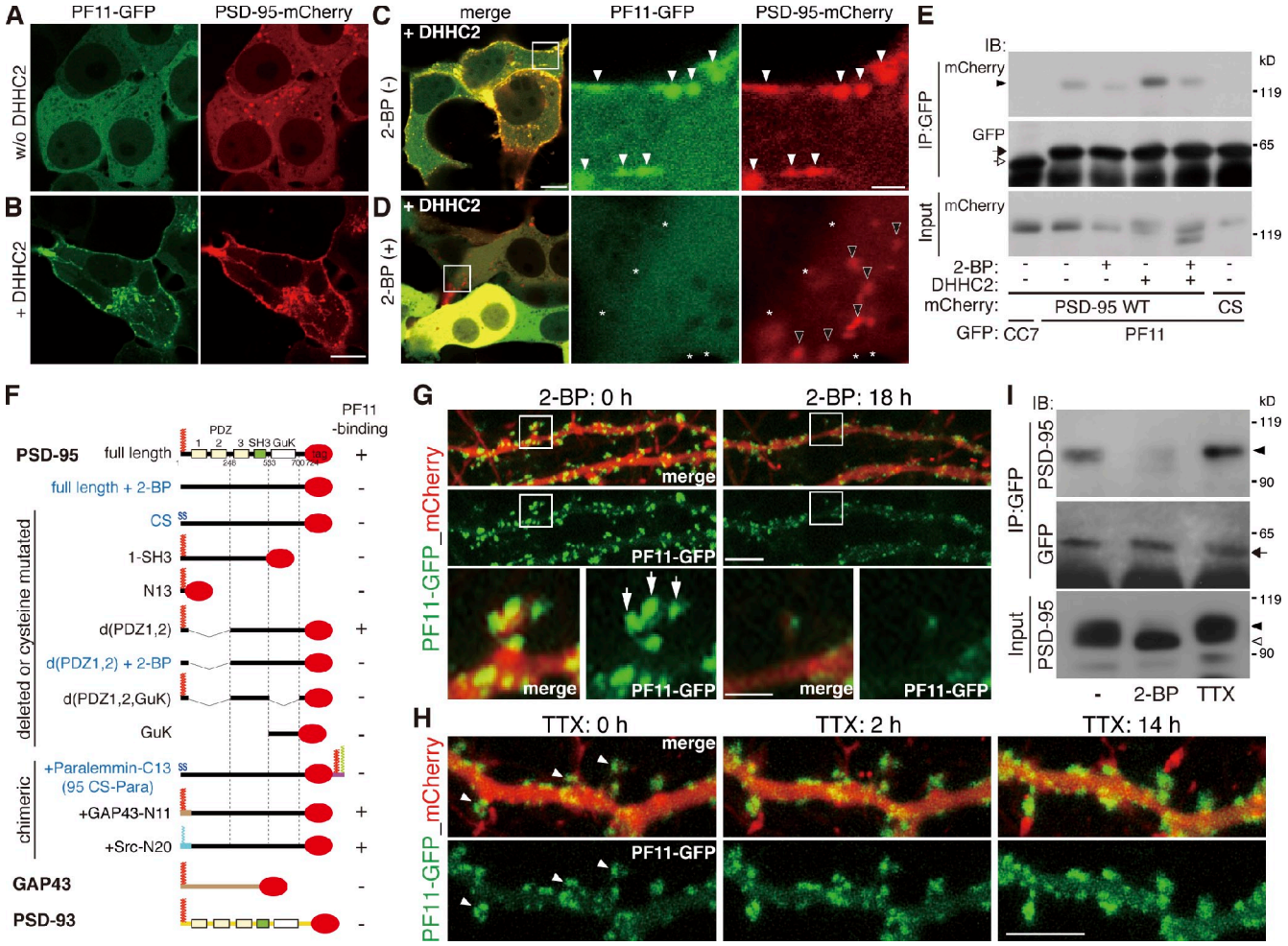

Figure 3. **PF11 as a conformation-specific intrabody for palmitoylated PSD-95.** (A–D) In the presence of DHHC2, PSD-95-mCherry and PF11-GFP were colocalized near the plasma membrane and on intracellular vesicular structures in HEK293T cells (B and C, white arrowheads). Treatment with 2-BP (100 µM, 8 h) dissociated PF11-GFP from the plasma membrane (asterisks) and intracellular aggregates of PSD-95-mCherry (D, black arrowheads). Bars, 10 µm (2 µm, magnified in C). (E) Immunoprecipitation (IP) of PF11-GFP from HEK293T cells. IB, immunoblotting. CC7, unrelated recombinant antibody; closed arrow, PF11-GFP; open arrow, CC7-GFP; closed arrowhead, PSD-95-mCherry. (F) PSD-95 constructs to test the specificity of PF11 binding using methods in Fig. 3, B and/or E. GuK, guanylate kinase domain; S, serine residues replacing palmitoyl cysteines. Red chain, palmitoyl; green, prenyl; blue, myristoyl groups. tag, mCherry or GFP. (G) Blockade of palmitoylation with 2-BP (100 µM, 18 h) dispersed synaptic labeling by PF11-GFP. Red, mCherry as a fill-in marker. Arrows, multiple subspine clusters. Bars, 5 µm (2 µm, magnified). (H) PF11-GFP tracked a synaptic increase of palmitoylated PSD-95 upon TTX treatment. Arrowheads, multicluster spines. Bar, 5 µm. (I) Immunoprecipitation of PF11-GFP from hippocampal neurons treated with 2-BP or TTX. Arrow, PF11-GFP. Closed and open arrowheads are as in Fig. 1 A.

(Fig. 3 F). These results strongly suggest that palmitoylation induces a change in PSD-95 conformation that can be sensed by PF11 and that PF11 recognizes a nonlinear epitope on the palmitoylated form of PSD-95 as reported for other antibodies (Vielemeyer et al., 2010). Fitting with this, hPF11 antibody was not applicable to Western blot of denatured samples (not depicted).

Next, to investigate the behavior of endogenous palmitoylated PSD-95, we expressed PF11-GFP in cultured hippocampal neurons. When visualized in fixed and in live neurons, PF11-GFP labeling was specifically enriched at discrete clusters in dendritic spines (Fig. 3, G and H; Fig. S1, H and I). PF11 intrabody expression did not inhibit the function of PSD-95 (Fig. S1, J and K) and could therefore be used to follow endogenous palmitoylated PSD-95 in intact neurons. Time-lapse imaging revealed a decrease in postsynaptic PF11-GFP signals over time upon 2-BP treatment (Fig. 3 G), thus visualizing in real time depalmitoylation of synaptic PSD-95. This decrease was not caused by photobleaching of GFP, as activity blockade by TTX under the same illumination conditions actually increased the postsynaptic PF11-GFP signal (Fig. 3 H), fitting with previous findings (Noritake et al., 2009). Additionally, immunoprecipitation of PF11-GFP from transfected neurons showed a decrease of PF11 binding to PSD-95 after 2-BP treatment and an increase after TTX treatment (Fig. 3 I). Taken together, these results indicate that PF11-GFP specifically binds to palmitoylated (and thus conformationally changed) PSD-95 in neurons and dissociates from PSD-95 upon depalmitoylation.

Subsynaptic nanodomains of palmitoylated PSD-95 as building blocks of the PSD

When analyzing 3D rendering of confocal image stacks in live neurons, we occasionally detected multiple small PF11-GFP clusters within a single dendritic spine (Fig. 3, G and H). Stimulated emission depletion (STED) super-resolution microscopy more

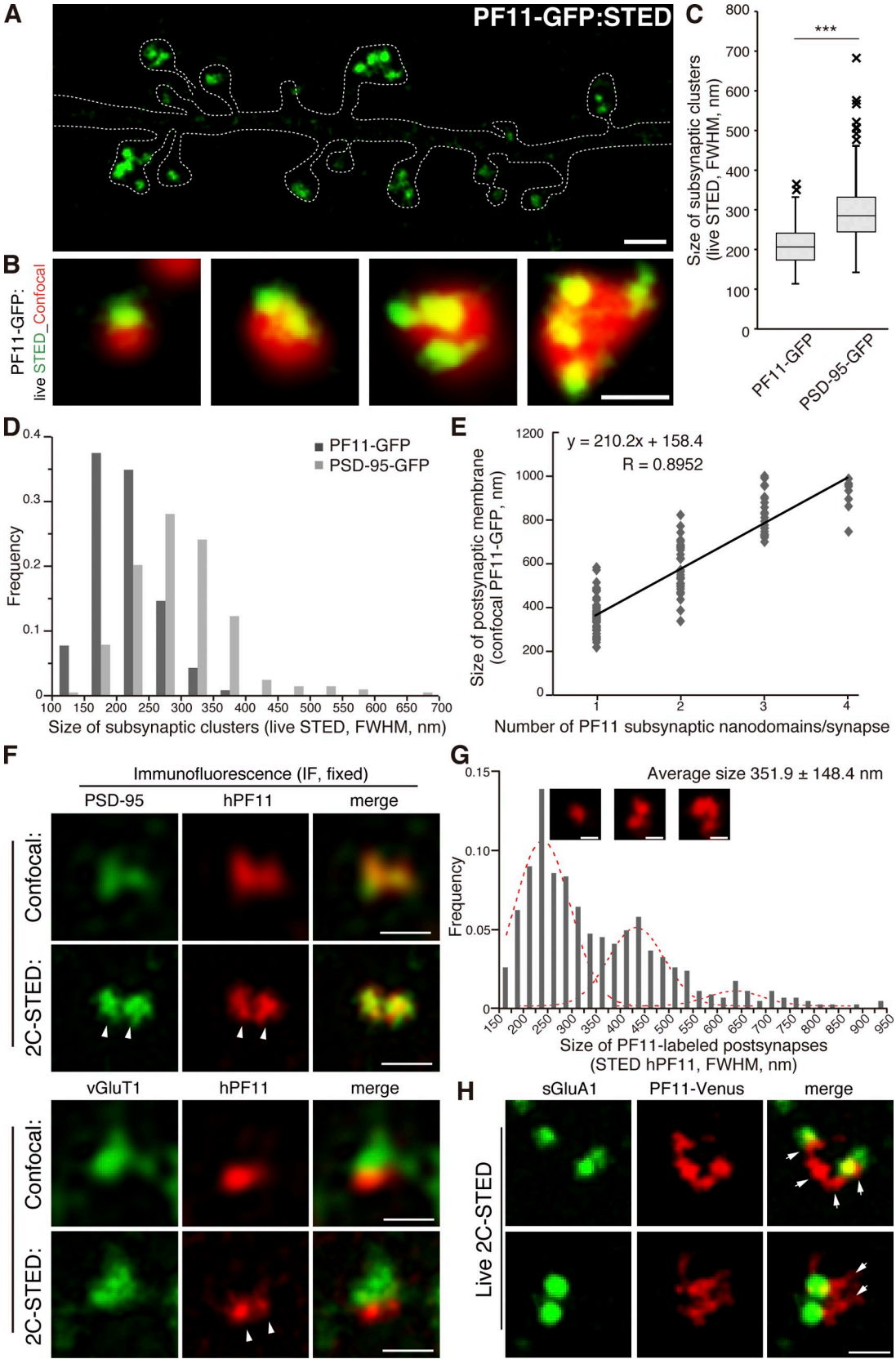

Figure 4. **Novel PSD-95 nanodomains as building blocks of postsynaptic membrane regions.** (A and B) Live-cell imaging of PF11-GFP by STED microscopy (green), but not by conventional confocal microscopy (red pseudocolor), efficiently detects multiple subspine clusters (1 to 4 clusters/spine) in neurons. Bars: (A) 1 µm; (B) 500 nm. (C and D) Size of subsynaptic nanodomains. Subsynaptic clusters of PF11-GFP and PSD-95-GFP visualized by live STED imaging were measured across the longest axis. Approximately 200 clusters were randomly selected from 10 live-imaging experiments. FWHM, full width at half maximum. ***, $P < 0.001$ by Student's *t* test. (E) The size of postsynaptic membrane regions (determined by confocal microscopy, red in B, according to

efficiently detected PF11-GFP labeling of these unique subspine structures in live neurons (Fig. 4, A and B). Conventional confocal microscopy did not readily resolve these subspine clusters; rather it visualized them as a single cluster (especially in the single-plane image acquisition mode), even when the same field was acquired by confocal and STED modes (Fig. 4 B and Fig. S2 A). Merged images of STED and confocal observation of PF11-GFP demonstrated that the conventional PSD (here, visualized by confocal PF11-GFP signals) represents, in fact, the apposition of several (up to >4) subsynaptic clusters of palmitoylated PSD-95 (visualized by STED PF11-GFP signals). Interestingly, the size of subsynaptic clusters was relatively uniform, irrespective of the number of clusters per synapse (Fig. 4, A and B). The average diameter of subsynaptic clusters, hereafter termed "subsynaptic nanodomains," was ∼200 nm (STED full width at half maximum [FWHM] 211.0 ± 48.8 nm, $n = 232$ clusters; Fig. 4 C). Size distribution histogram for PF11-labeled nanodomains was symmetric without apparent longer size tails (Fig. 4 D). Nanodomains in the postsynaptic membrane were separated from each other by narrow gaps (less than ∼200 nm, i.e., below the resolution of confocal microscopy; Fig. 4, A and B; Fig. S2 A). Based on these observations, we hypothesized that PSD-95 nanodomains represent subdomains of the PSD and that their number could be a determinant of PSD size. Indeed, there was a good correlation between the number of PF11-labeled nanodomains per synapse and the overall size of a given postsynaptic membrane as determined by confocal PF11-GFP (correlation coefficient R = 0.8952; Fig. 4 E). Furthermore, live-cell STED imaging also revealed that conventional PSD-95-GFP existed in similar subsynaptic clusters within spines (Fig. S2 A), although PSD-95-GFP–labeled subsynaptic clusters were larger (STED FWHM 295.3 ± 78.9 nm, $n = 203$ clusters) than PF11-labeled (endogenous PSD-95) nanodomains (Fig. 4, C and D).

We next performed dual-color STED imaging (2C-STED) of fixed hippocampal neurons by hPF11 and conventional PSD-95 immunofluorescence (Fig. 4 F). STED imaging of hPF11, but not confocal imaging, resolved subsynaptic nanodomains in fixed neurons, despite the reduced resolution that was most likely caused by fixation-induced structure shrinkage (Fig. 4 F and Fig. S2 B). As expected, hPF11 signals overlapped with total PSD-95 signals, which also showed nanodomain organization (Fig. 4 F, top panels). Co-staining with vGlut1 showed that individual nanodomains of the postsynapse faced a single presynaptic terminal (Fig. 4 F, bottom panels). The size of the hPF11-labeled postsynaptic membrane region was defined as the FWHM across the longest points of the STED hPF11 signal (Fig. S2 B) and ranged widely from 150 nm to ∼1 µm with a mean diameter of 351.9 ± 148.4 nm ($n = 469$ synapses; Fig. 4 G). This value was compatible with the PSD size previously reported in an electron microscopic analysis (mean size, ∼360 nm; Petersen et al., 2003; Arellano et al., 2007). The size distribution showed the strongest frequency peak at around 200–250 nm and could be fitted with at least two additional Gaussian peaks at ∼420 and ∼625 nm (Fig. 4 G, red dashed curves). A similar size distribution had been previously described for PSDs in an electron microscopic analysis (Arellano et al., 2007; Swulius et al., 2010). It is conceivable that the PF11-labeled postsynaptic structure may represent the PSD, and that the PSD may be composed by a set of palmitoylated PSD-95–enriched subdomains with diameters of ∼200 nm.

Because PSD-95 anchors AMPARs at the postsynapse through interaction with stargazin and related transmembrane AMPAR regulatory proteins (TARPs; Tomita et al., 2003; Elias and Nicoll, 2007), we investigated whether individual postsynaptic nanodomains associate with the endogenous GluA1 AMPAR subunit. Neurons expressing PF11-Venus were live-labeled with an anti-GluA1 antibody targeted to an extracellular epitope, after which PF11-Venus and surface-expressed AMPARs were visualized using live-cell 2C-STED imaging. AMPAR clusters appeared to be associated with distinct nanodomains (Fig. 4 H; also see Fig. 9 A).

Continuous palmitate cycling on PSD-95 nanodomains driven by local palmitoylating activity

We then examined the dynamics of PSD-95 palmitoylation and where in neurons palmitoylation, depalmitoylation, and eventually repalmitoylation of PSD-95 occur. We compared fluorescence recovery rates after photobleaching (FRAP) of PF11-GFP and PSD-95-GFP at individual clusters within spines. In agreement with previous reports (Kuriu et al., 2006; Blanpied et al., 2008), the recovery rate of PSD-95-GFP was very slow (14.5 ± 2.6% recovery at 1 h after bleaching; Fig. 5, A, C, and D; Video 1). In parallel, we performed the FRAP of PF11-GFP. The recovery rate of PF11-GFP clusters was much faster (55.7 ± 8.8% recovery at 1 h after bleaching; Fig. 5, A–D; Video 2), and the recovered PF11-GFP fluorescence appeared within the narrowly focused area at the original locations of the nanodomains in a spine (Fig. 5 A, right magnified images, and Video 2). Part of this recovery can be attributed to dynamics of PF11 binding to its target, while another part may be due to cycling of PSD-95 between palmitoylated and depalmitoylated forms. However, this recovery was completely inhibited by treatment with 2-BP at any time points during the recovery period (Fig. 5, A, C, and D), indicating that it mostly depends on active palmitoylation of PSD-95. In contrast, 2-BP treatment did not affect the recovery of PSD-95-GFP, indicating that arrival of new PSD-95-GFP in the spine does not depend on on-going palmitoylation. Thus, on

diameter at the longest axis) correlates well with the number of PF11-labeled subsynaptic nanodomains (determined by STED, green in B). 130 postsynapses from 5 live neurons were analyzed. (F) Dual-color STED (2C-STED) analysis of fixed neurons. Postsynaptic hPF11 labeling (red pseudocolor) shows nanodomain structures (arrowheads), overlapping with total PSD-95 labeling (green pseudocolor, top panels) and apposed to presynaptic vGlut1 labeling (green pseudocolor, bottom). The same fields were sequentially imaged in the confocal mode. Bars, 500 nm. (G) The size of PF11-labeled postsynaptic regions was measured by STED microscopy, as described in Fig. S2 B for a representative image from F, and the frequency histogram is shown. Peaks by the Gaussian approximation centered at 225, 420, and 625 nm are shown in red dashed lines. In total, 450 clusters from 6 neurons (three independent experiments) were analyzed. Representative regions with one, two, and three nanodomains are shown (insets). Bars, 200 nm. (H) Individual nanodomains (red pseudocolor) in a spine are associated with AMPARs (green pseudocolor). sGluA1, surface-expressed GluA1. Arrows, nanodomains labeled by PF11-Venus. Bar, 500 nm.

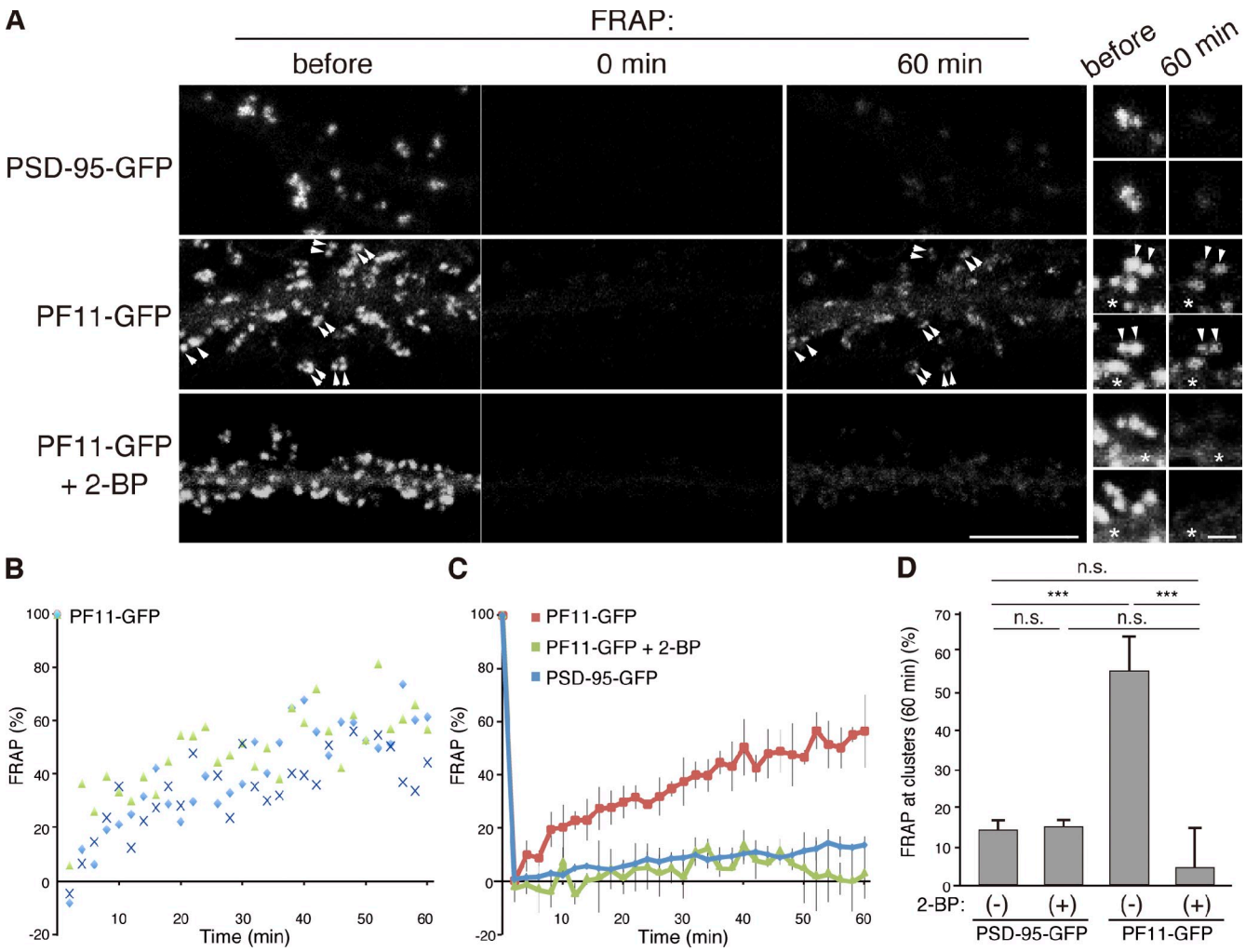

Figure 5. **Continuous palmitate cycling on PSD-95 nanodomains is mediated by local palmitoylating activity.** (A) Dendritic regions of transfected hippocampal neurons were bleached, and then the fluorescent recovery of PSD-95-GFP or PF11-GFP at the individual clusters was monitored. Right, representative magnified images before bleaching and at 60 min after bleaching. Note that the recovered PF11-GFP kept its initially distinguished nanodomain locations (arrowheads). Asterisks, diffuse fluorescent signals of PF11-GFP in dendritic shaft that were subtracted from the FRAP at the clusters. Bars: (left) 5 µm; (right) 0.5 µm. (B) Sample FRAP of PF11-GFP at subsynaptic clusters. (C) Average FRAP of PF11-GFP (red), PF11-GFP treated with 2-BP (green), and PSD-95-GFP (blue). *n* = 3 experiments (5–6 clusters/experiment). (D) Fluorescence recovery of PSD-95-GFP and PF11-GFP at 60 min after bleaching in the presence or absence of 2-BP. ***, P < 0.001 by one-way ANOVA with post-hoc Tukey's test (*n* = 3 experiments [5–6 clusters/experiment]).

the one hand, the total pool of PSD-95 appeared mostly retained within the same spine, barely being exchanged during a 1-h observation, and on the other hand, the same pool of PSD-95 in a given spine was continuously cycling between (re)palmitoylated and depalmitoylated forms. It is conceivable that local palmitoylating activity at the postsynaptic membrane defines the precise locus of PSD-95 nanodomains. Accordingly, *N*-myristoylated PSD-95 (Src-N20/PSD-95-GFP), which is irreversibly lipidated and cannot be affected by palmitoyl enzymes, is membrane targeted in neurons but is not efficiently clustered at dendritic spines (Fig. S3 A), as described previously (Craven et al., 1999).

DHHC2, a plasma membrane–inserted palmitoylating enzyme, is required for postsynaptic PSD-95 nanodomain formation

Because DHHC2, a major PSD-95 PAT, is located on vesicle structures in dendrites and often in dendritic spines (Noritake et al., 2009), we explored the possibility that DHHC2 would palmitoylate PSD-95 locally on the spine membrane to generate postsynaptic PSD-95 nanodomains and define the site of PSD organization. To detect DHHC2 on the cell surface, a hemagglutinin (HA) tag was inserted in the second luminally oriented loop of the enzyme (DHHC2-$_{lum}$HA, Fig. 6 A). Cell surface staining with an anti-HA antibody detected DHHC2 expressed at the plasma membrane as clusters in dendritic spines (Fig. 6 B). Cell surface expression of DHHC2 was observed before in PC12 cells (Greaves et al., 2011). In contrast, Golgi-localized DHHC3, another subfamily member of PSD-95 PATs, was not detected on the cell surface. Endogenous DHHC2 was found as discrete small puncta in the hPF11-stained postsynaptic region (at the center of two nanodomains; Fig. 6 C). GFP-DHHC2 was localized mainly on transferrin receptor–positive recycling endosomes in the dendrite (Fig. 6 D, left), as described in PC12 cells (Greaves et al., 2011) and juxtaposed to PSD-95-mCherry clusters in the spines (Fig. 6 D, middle). Live-cell imaging using super-ecliptic pHluorin (SEP)–tagged

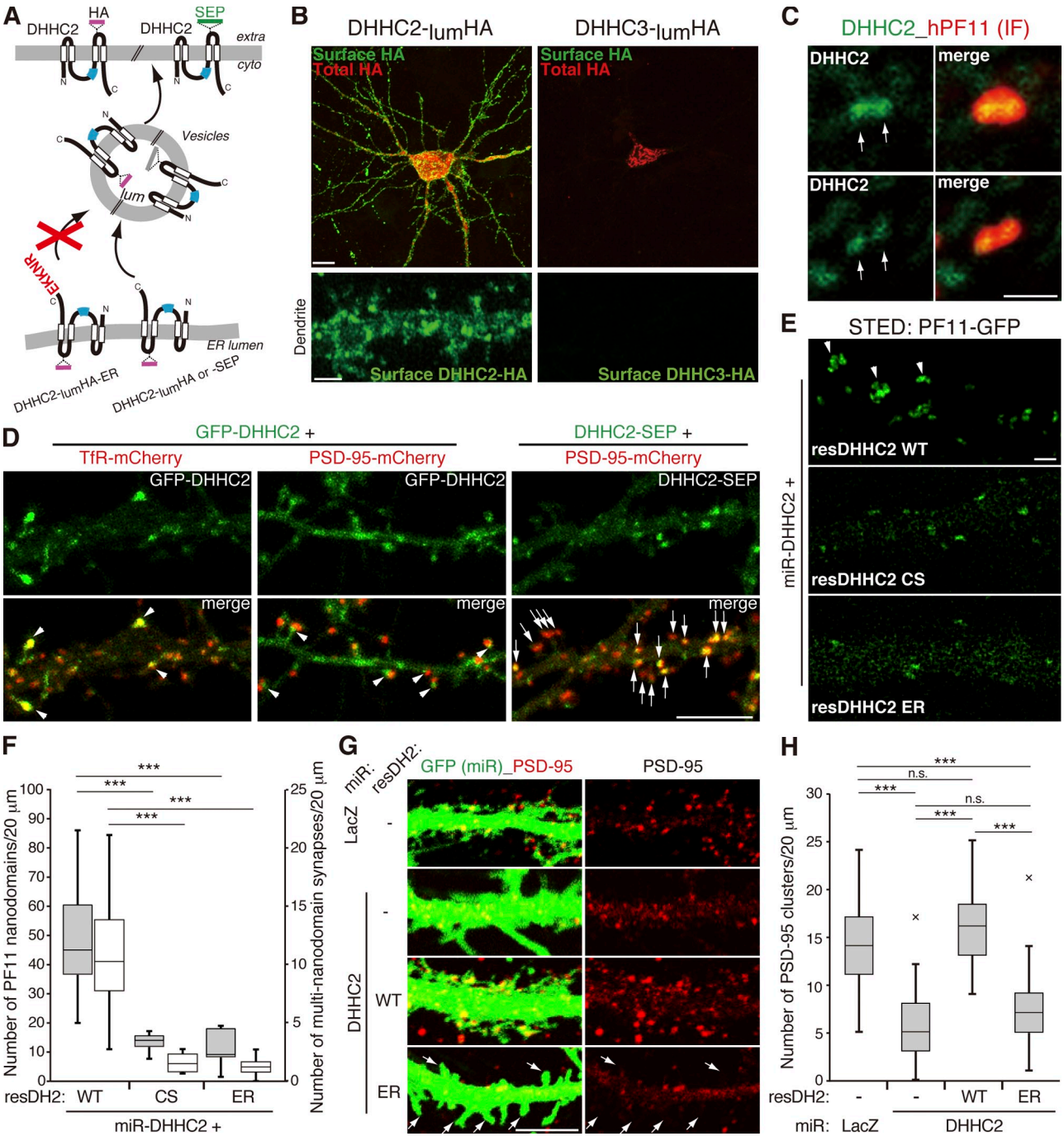

Figure 6. **Surface-expressed DHHC2 is essential for generation of postsynaptic nanodomains.** (A) DHHC2 constructs used. EKKNR, an ER-retention signal; SEP, super-ecliptic pHluorin. Blue boxes, DHHC catalytic domain. extra, extracellular space; cyto, cytoplasm; lum, lumen. (B) Surface-expressed and total DHHC-HA are shown in green and red, respectively. Bars: (top) 10 µm; (bottom) 2 µm. (C) Endogenous DHHC2 (green) exists as small discrete clusters (arrows) at the center of hPF11-stained postsynaptic regions (red) in a spine. Bar, 1 µm. (D) Endosomal (arrowheads) and synaptic membrane localization (arrows) of DHHC2. GFP-DHHC2 or DHHC2-SEP was coexpressed with TfR-mCherry or PSD-95-mCherry. Bar, 5 µm. (E and F) Hippocampal neurons were transfected with PF11-GFP-miR-DHHC2 (for co-cistronic expression) and miRNA-resistant DHHC2 (resDHHC2-WT, CS, or ER), and live-imaged using STED microscopy. PF11-GFP–labeled nanodomains (gray boxes) and multi-nanodomain synapses (E, arrowheads; white boxes) were counted (F). In total, 35 (WT), 4 (CS), and 11 (ER) dendrites from two or three independent experiments were analyzed. Bar: (E) 1 µm. (G and H) miRNA against DHHC2 (marked by EmGFP) was expressed with resDHHC2 WT or –ER. Neurons were stained using a conventional PSD-95 antibody (red) and imaged by confocal microscopy. miLacZ indicates a control miRNA. Arrows denote PSD-95-negative dendritic spines/filopodia (G). Approximately 50 dendrites from 2 independent experiments were analyzed (H). resDH2, resDHHC2. ***, $P < 0.001$, by one-way ANOVA with post-hoc Tukey's test (F and H). Bar: (G) 5 µm.

DHHC2, which allows to specifically monitor surface-expressed DHHC2, showed the complete colocalization of surface DHHC2 with PSD-95–mCherry clusters at the postsynaptic membrane (Fig. 6 D, right).

To explore whether the surface expression of DHHC2 is necessary for the generation of postsynaptic nanodomains of PSD-95, we generated a DHHC2 construct with an ER-retention signal (-EKKNR) at its C terminus (DHHC2 ER; Fig. 6 A).

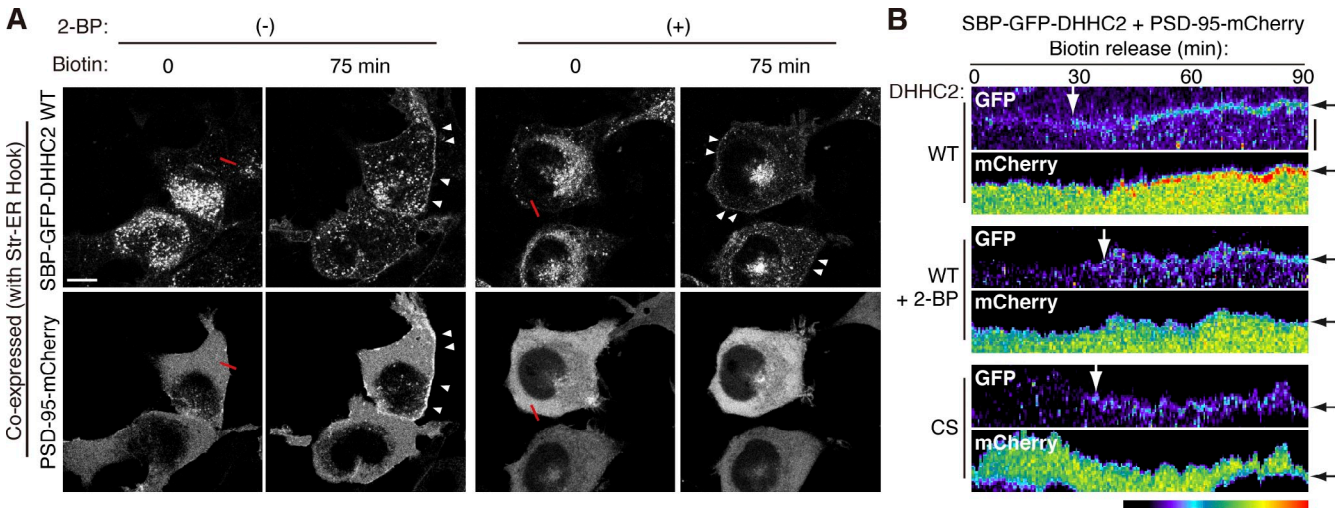

Figure 7. **DHHC2 directly nucleates PSD-95 assembly at the plasma membrane through local palmitoylation.** (A) HEK293T cells were cotransfected with a bi-cistronic RUSH vector containing streptavidin-li (Str-ER Hook) and streptavidin-binding peptide (SBP)-GFP-DHHC2 as well as PSD-95-mCherry. Synchronized release of DHHC2 from the ER was induced by the addition of biotin with or without 2-BP. Arrowheads denote signals at the plasma membrane. Bar, 10 µm. (B) Kymograph analysis. The fluorescence intensities of GFP and mCherry were measured along red lines in A. White arrows indicate the timing when DHHC2 arrived at the plasma membrane. Black arrows indicate the position of the plasma membrane (at 90 min). CS, inactive DHHC2. Bar, 2.5 µm.

DHHC2 ER accumulated at the ER in the cell body and dendrites but was never detected at the cell surface of transfected neurons (Fig. S3 B). When knockdown-resistant DHHC2 ER or catalytically inactive DHHC2 CS was expressed in neurons in which DHHC2 was knocked down, the number of PF11-GFP–labeled subsynaptic nanodomains and the number of multi-nanodomain synapses (i.e., larger postsynapses) were greatly reduced relative to WT DHHC2-expressing neurons (Fig. 6, E and F). Furthermore, knockdown of DHHC2 significantly reduced the number of PSD-95–positive clusters, representative of PSDs. This reduction was completely rescued by expressing knockdown-resistant DHHC2 WT, but not DHHC2 ER (Fig. 6, G and H). Thus, plasma membrane–inserted DHHC2 is essential for the formation of PSD-95 nanodomains, and thereby regulates the number and size of postsynaptic membrane regions.

Plasma membrane insertion of DHHC2 triggers specific PSD-95 accumulation at the plasma membrane

To show a direct causative relationship between DHHC2 plasma membrane targeting and subsequent PSD-95 accumulation, we took advantage of our recently developed synchronized secretion system (retention using selective hooks [RUSH]; Boncompain et al., 2012) that allowed the efficient synchronized trafficking of DHHC2 to the plasma membrane. As illustrated in Fig. S4 A, streptavidin-binding peptide (SBP)–fused GFP-DHHC2 (SBP-GFP-DHHC2) was hooked at the ER by the interaction with the streptavidin (Str)-fused ER-resident protein Ii. Upon addition of biotin, SBP-GFP-DHHC2 was acutely released from the ER, entered the Golgi apparatus (~10 min after biotin addition), and got sorted into the secretory pathway to its final destination, the plasma membrane (visible around ~30 min; Fig. 7 A, top left; Video 3). Using this RUSH system we coexpressed PSD-95-mCherry with SBP-GFP-DHHC2. Time-lapse imaging and its kymograph analysis clearly show that (1) before biotin addition, DHHC2 accumulated at the ER, and PSD-95-mCherry was distributed diffusely in the cytoplasm; and that (2) biotin-induced synchronized trafficking of SBP-EGFP-DHHC2 to the plasma membrane caused subsequent specific accumulation of PSD-95 at the same plasma membrane regions (Fig. 7, A [left] and B; Video 3). This effect of DHHC2 on PSD-95 accumulation requires its palmitoylating activity, as PSD-95 accumulation was not observed in the presence of 2-BP (Fig. 7, A [right] and B; Video 4) or when catalytically inactive DHHC2 (CS) was expressed (Fig. 7 B and Video 5). Similarly, forced engagement of DHHC2-$_{lum}$HA with anti-HA antibody on the cell surface (Fig. S4 B) induced PSD-95 recruitment in COS7 cells and neurons (Fig. S4, C–E). Thus, plasma membrane–targeted DHHC2 catalyzes the local PSD-95 palmitoylation and then specific PSD-95 accumulation at the plasma membrane.

Changes in synaptic activity alter the core postsynaptic architecture through the local palmitoylating machinery

We next asked how altered palmitoyl cycling on postsynaptic PSD-95 affects the postsynaptic structure. We stimulated cultured neurons with 90 mM KCl for 5 min, which activates synaptic glutamate receptors and enhances depalmitoylation of PSD-95 (Kang et al., 2004). Neurons were then stained triply with hPF11, PSD-95, and vGlut1 antibodies. Acute depolarization robustly reduced the fluorescence intensity of hPF11-stained postsynaptic clusters and modestly reduced PSD-95 cluster intensity (Fig. 8, A and B). This reduction in hPF11 intensity was reversed when high K^+ medium was replaced with basal medium and neurons were incubated for 1 h. Importantly, STED microscopy revealed that upon depolarization, signals of total PSD-95 that overlapped with nanodomains of PF11-labeled postsynapses were reduced, and stronger PSD-95 signals were observed additionally in areas independent of nanodomain locations (Fig. 8 C and Fig. S5 A). Approximately 30% of observed

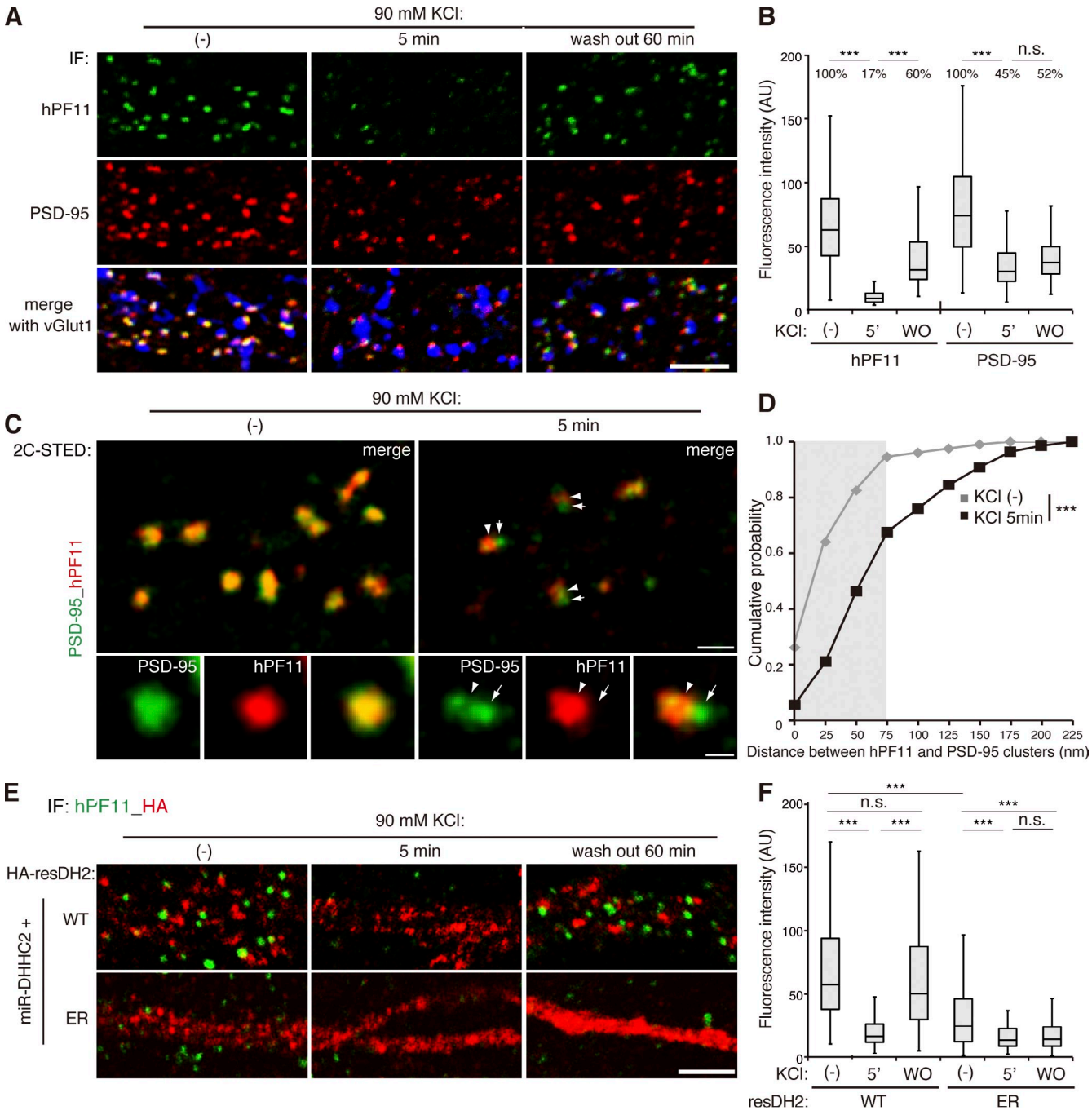

Figure 8. **Changes in synaptic activity remodel postsynaptic PSD-95 nanodomains through local DHHC2 activity.** (A and B) Neurons were treated with 90 mM KCl for 5 min and recovered for 60 min in the basal medium (wash out, WO). Neurons were stained triply with hPF11 (green), PSD-95 (red), and vGlut1 (blue) antibodies, and the confocal fluorescence intensities of green and red channels at PSD-95–positive clusters were measured. In total, 170–240 clusters from three neurons were analyzed. ***, $P < 0.001$ by one-way ANOVA with post-hoc Tukey's test (B). Bar, 5 µm. (C and D) Neurons treated with high K^+ were analyzed by 2C-STED imaging of PSD-95 (green pseudocolor) and hPF11 (red pseudocolor), and the distance between the peaks with the highest intensity of hPF11 (arrowheads) and PSD-95 (arrows) clusters was measured (as described in Fig. S5 A). The brightness of magnified images with KCl treatment is enhanced. Gray region in D indicates the subresolution range for STED imaging. In total, 150–200 clusters from 10 neurons (two independent experiments) were analyzed. ***, $P < 0.001$ by Student's *t* test (D). Bars, 500 nm (200 nm, magnified). (E and F) Neurons were cotransfected with miR-DHHC2 and HA-resDHHC2-WT or ER (red), and treated as in (A). The confocal fluorescence intensity of hPF11 (green) overlapped with vGlut1 (not depicted) was measured. In total, 230–420 clusters from 8 neurons (three independent experiments) were analyzed. ***, $P < 0.001$ by one-way ANOVA with post-hoc Tukey's test. Bar, 5 µm.

PSD-95 signals were >∼100 nm away from hPF11-labeled postsynaptic areas in the high K^+ condition, whereas they were overlapping under the basal condition (>95% were within subresolution distance, gray region in the graph; Fig. 8 D and Fig. S5, A and B). Furthermore, 2C-STED imaging using bassoon co-staining, a marker protein of the presynaptic active zone, supports the displacement of some populations of PSD-95, but not palmitoylated PSD-95, from the synaptic sites by high

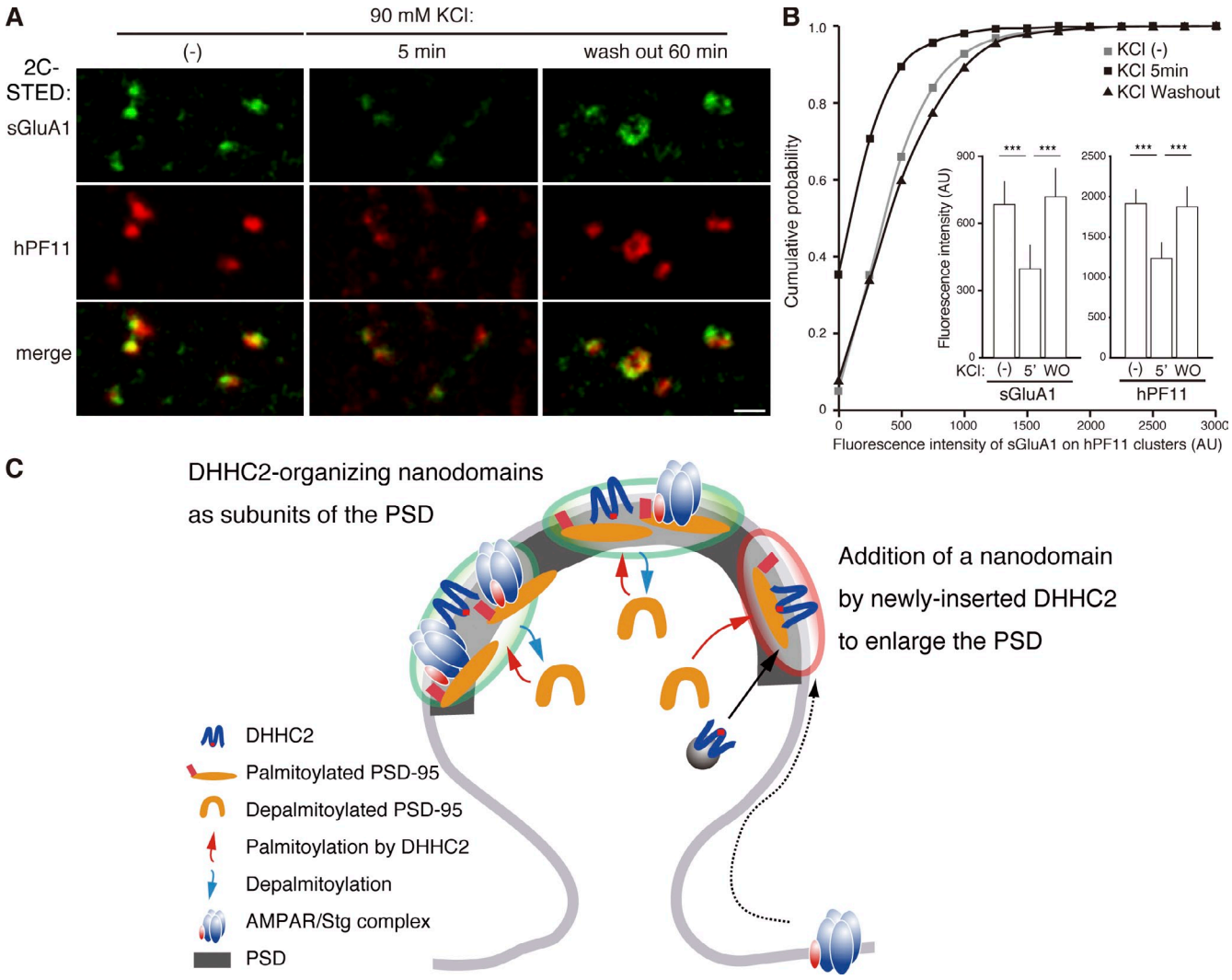

Figure 9. **Synaptic activity regulates the association of AMPARs with postsynaptic nanodomains.** (A and B) Neurons were treated with 90 mM KCl for 5 min and recovered for 60 min. Neurons were analyzed by 2C-STED imaging of surface GluA1 (A, green pseudocolor) and hPF11 (A, red pseudocolor), and the maximum intensity of surface AMPARs on PF11-labeled nanodomains was measured (B). In total, ∼1,000 clusters from 8–12 neurons (two independent experiments) were analyzed. ***, $P < 0.001$ by one-way ANOVA with post-hoc Tukey's test. Bar, 500 nm. (C) A DHHC2-mediated subdomain model for PSD (re)organization: organization of nanodomains through local palmitoylation/depalmitoylation cycles. See Discussion.

K^+ (Fig. S5, C–E). In addition, the size of postsynaptic membrane region labeled with hPF11 (as measured in Fig. 4 G) was significantly reduced by high K^+ (STED FWHM 242.4 ± 99.5 nm, n = 398 clusters; Fig. S5 F). Thus, PSD-95 is rapidly depalmitoylated and repalmitoylated in response to changes in synaptic activity, and is locally displaced from the postsynaptic membrane within the spine upon depalmitoylation.

We next tested whether this activity-regulated remodeling of postsynaptic PSD-95 clusters in dendritic spines involves repalmitoylation through local DHHC2 activity. When wild-type DHHC2 was reexpressed in the DHHC2 knockdown neurons, it was found at dendritic spines, and the postsynaptic hPF11 intensity efficiently recovered within 1 h after removal of the high K^+ medium (Fig. 8, E and F). In contrast, when neurons were complemented with the mutant DHHC2 ER that was retained at the dendritic ER and hardly detected in the spine, the postsynaptic hPF11 signal intensity was already significantly reduced in the basal state, and further reduced by high K^+. Importantly, it did not recover after removal of the high K^+ medium. Thus, postsynaptic PSD-95 clusters are dynamically remodeled on a nanoscale level by synaptic activity–regulated palmitoyl cycling on PSD-95, and spine membrane–inserted DHHC2 ensures this exquisite spatial organization of postsynaptic membrane regions.

We finally investigated whether changes in synaptic activity affect the association of AMPARs with postsynaptic nanodomains. We found that high K^+–induced depolarization significantly reduced the fluorescence intensity of surface AMPARs on hPF11-labeled postsynaptic clusters by 2C-STED imaging, and that this reduction was reversed upon washing out of high K^+ medium (Fig. 9, A and B).

Discussion

The exact mechanism involved in the initiation, maintenance, and remodeling of PSD organization remains controversial. Here, we propose a subdomain model for the PSD organization

(Fig. 9 C). The PSD may not be a region with randomly distributed PSD-95 molecules, but rather an ordered assembly of PSD-95–based subdomains, initiated by local DHHC2 activity. A set comprised of synaptic DHHC2 and an unidentified depalmitoylating enzyme drives this intra-spine palmitoyl cycle to produce a spatially confined dynamic equilibrium of PSD-95 location within the spine. Such a rapid intra-spine palmitoyl cycling may prevent lateral diffusion of membrane-bound PSD-95 to other regions of the spine membrane. PSD-95 nanodomains would thus serve as a platform for supra-molecular assemblies including stargazin/AMPARs, NMDA receptors, neuroligin, SynGAP, kalirin-7, and GKAP scaffolds, which in turn would recruit Shank–Homer complexes leading to mature PSDs (Kim and Sheng, 2004; Hayashi et al., 2009). Furthermore, enhanced synaptic activity causes rapid depalmitoylation of PSD-95, locally dissociates PSD-95 from postsynaptic nanodomains, and reduces the size of postsynaptic nanodomains. This process is reversible through DHHC2-mediated repalmitoylation of the same pool of PSD-95 molecules. Thus, the DHHC2-mediated subdomains should provide the PSD with the intrinsic property to rapidly reorganize its structure and molecular composition in response to changes in synaptic activity. Given that palmitoylated PSD-95 displays a particular conformation sensed by PF11 (see also Nakagawa et al., 2004), this conformation may enable specific interactions between PSD-95 and some of its partners within the PSD. In fact, we observed that the association of postsynaptic nanodomains with AMPARs was also regulated by synaptic activity. Taking into account previous studies (Tomita et al., 2004; Sumioka et al., 2010), it is conceivable that PSD-95 palmitoylation, stargazin phosphorylation, and the ligand-induced allosteric mechanism for AMPARs cooperatively regulate the dynamic interaction of AMPARs with the PSD.

Another feature of the subdomain model is that the number of assembled PSD-95 nanodomains determines the size of the PSD. We found that large synapses are composed of more than one nanodomain (Fig. 4, E and G), and that loss of plasma membrane DHHC2 reduces the number of large synapses with multiple nanodomains (Fig. 6, E and F). When additional DHHC2 is inserted into the spine membrane, it would locally catalyze PSD-95 palmitoylation and create a new nanodomain (Fig. 9 C, a new domain in red), which leads to increased size of the PSD.

To date, the exact subcellular location of protein palmitoylation has not been completely elucidated. Recent studies on DHHC palmitoylating enzymes have helped answer this question. PSD-95 is modified by two different subfamilies of DHHC proteins, DHHC3 and DHHC2 (Fukata et al., 2004; Noritake et al., 2009). In neurons, DHHC3 is localized exclusively at the Golgi apparatus in the cell body (Noritake et al., 2009; Tsutsumi et al., 2009). In contrast, DHHC2 is found on transport vesicles in dendrites far from the cell body (Noritake et al., 2009) and even inserted into dendritic spine membranes (Fig. 6). The present study clearly showed a direct causal relationship between DHHC2 plasma membrane targeting and local PSD-95 palmitoylation. Thus, the site of protein palmitoylation is not restricted to endomembranes. Strikingly, we showed that ER-localized DHHC2 was not able to induce membrane recruitment of PSD-95 (Fig. 7). The plasma membrane, which is the final destination of trafficked palmitoylated proteins, can also function as an active, and specific, palmitoylation locus. A two-stage regulation of protein palmitoylation at endo- and plasma membranes would help to efficiently establish and maintain specific protein assembly sites at the plasma membrane. Importantly, 23 types of DHHC palmitoylating enzymes with divergent and overlapping substrate specificities have been described in mammalian cells (Fukata and Fukata, 2010). In future research, the precise cellular mechanisms that allow targeting of individual DHHC enzymes should be elucidated.

In summary, we discovered novel subdomains of the PSD, and elucidated their activity-responsive regulatory mechanism through DHHC2-dependent palmitoylation. Our proposed model will contribute to understanding dynamic features of the PSD and other specialized membrane regions in polarized cells.

Materials and methods

Materials

The following antibodies were used: rabbit polyclonal antibodies to HA (Y-11; Santa Cruz Biotechnology, Inc.), mCherry/dsRed (MBL), GluA1 (PC246; EMD Millipore), vGlut1 (for 2C-STED; Synaptic Systems), and bassoon (Synaptic Systems); a rat monoclonal antibody to HA (3F10; Roche); mouse monoclonal antibodies to PSD-95 (MA1-046; Thermo Fisher Scientific), HA (16B12; Covance), and DHHC2 (Noritake et al., 2009), as well as guinea pig polyclonal antibodies to vGlut1 (AB5905; EMD Millipore) and vGlut2 (AB2251; EMD Millipore). A rabbit polyclonal antibody to GFP was raised against GST-GFP (aa 1–239) and affinity purified.

The following reagents were used: 2-bromohexadecanoic acid (2-bromopalmitate, 2-BP; Fluka), tetrodotoxin (TTX; Nacalai Tesque), picrotoxin (Sigma-Aldrich), D-biotin (Sigma-Aldrich), and anisomycin (EMD Millipore).

Plasmid constructions

To obtain the antigen for antibody screening, pGW1-PSD-95-GFP-TEV-$(Gly)_7$-PSTCD was generated by a standard PCR method. The PSTCD tag (McCormick et al., 2006) was extracted from the pPinpoint plasmid (Promega). In brief, the tobacco etch virus (TEV) protease recognition site (ENLYQG), a $(Gly)_7$ linker, and a biotin acceptor peptide (*Propionibacterium shermanii* transcarboxylase domain [PSTCD]; GenBank/EMBL/DDBJ accession no. AJ535201) were tandemly added to the C terminus of PSD-95-GFP. The single-chain fragment Vs (scFVs), PF11 and CC7, were subcloned into pEGFP-N3 or pmCherry-N3 and used for expression in HEK293T cells. PF11-GFP and CC7-GFP were then subcloned into pCAGGS for neuronal expression. Rat PSD-95 (aa 1–724) and PSD-93(β) cDNAs were subcloned into pGW1-GFP vector. pGW1-PSD-95 CS-GFP was generated using site-directed mutagenesis. PSD-95 1-SH3 (aa 1–495); N13 (aa 1–13; El-Husseini et al., 2000a); d(PDZ1,2) lacking aa 65–247; d(PDZ1,2; GuK) lacking aa 533–699 from PSD-95 d(PDZ1,2); and GuK (aa 533–699) were generated by PCR and subcloned into pGW1-GFP vector. pGW1-PSD-95 CS-GFP/Para was generated by appending a synthetic DNA encoding the prenylation motif of paralemmin (DMKKHRSKSCSIM in aa) to the C terminus of PSD-95 CS-GFP (El-Husseini Ael et al., 2002). pGW1-GAP43 N11/PSD-95-GFP and pGW1-Src N20/PSD-95-GFP were constructed by replacing the N-terminal palmitoylation motif of PSD-95 (aa 1–12 or aa 1–20) with the synthetic DNA encoding a fatty acylation motif of GAP43 (aa 1–11; dually palmitoylated) or Src (aa 1–20; myristoylated), respectively. Mouse DHHC2 and DHHC3 (with N-terminal, cytoplasmic HA-tag) were isolated by RT-PCR from mouse brain total RNAs and subcloned into pEF-Bos-HA vector (Fukata et al., 2004). To generate DHHC2-$_{lum}$HA and DHHC3-$_{lum}$HA in which the HA epitope (YPYDVPDYA) is placed in the second luminally oriented loop, HA was inserted with a Gly–Gly linker between 198T and 199N of DHHC2 and between 203T and 204K of DHHC3, respectively. DHHC2-$_{lum}$SEP was generated by inserting SEP cDNA between 198T and 199N of DHHC2. DHHC2-ER was obtained by adding the ER-retention signal (EKKNR) of DHHC6 to its C terminus (Gorleku et al., 2011).

PSD-95 was knocked down by transfecting pLLox3.7-shPSD-95 together with a GFP reporter (American Type Culture Collection; Elias et al., 2006). For molecular replacement experiments, shRNA-resistant PSD-95 constructs (resPSD-95 WT, CS) that have four different nucleotides in the target sequences were generated using site-directed mutagenesis (5′-TCACAATAATAGCCCAGTATA-3′ [changed nucleotides are underlined]; Noritake et al., 2009). Knockdown of DHHC2 was performed using the miR-RNAi system with EmGFP or mCherry as reporters (Invitrogen), and miRNA-resistant DHHC2 constructs (resDH2) were used for molecular replacement experiments as described previously (Noritake et al., 2009). In Fig. 6, E and F, PF11-GFP was replaced with EmGFP reporter for the cocistronic expression of PF11-GFP and miR-DHHC2.

For RUSH assay, streptavidin-fused Ii and SBP-fused GFP-DHHC2 were used for the ER hook and the reporter, respectively. These genes were expressed under the same CMV promoter and were separated by a synthetic intron and an internal ribosome entry site (Boncompain et al., 2012).

R.Y. Tsien (University of California, San Diego, La Jolla, CA), G. Miesenboeck (University of Oxford, Oxford, England, UK), and V.V. Verkhusha (Albert Einstein College of Medicine, Bronx, NY) provided us with cDNAs encoding mCherry (Shaner et al., 2005), SEP (Miesenböck et al., 1998), and transferrin receptor (Subach et al., 2009), respectively. PSD-95 deletion and chimeric constructs were provided by D.S. Bredt (Johnson & Johnson, San Diego, CA). All PCR products were analyzed by DNA sequencing (Functional Genomics Facility, NIBB, Aichi, Japan).

Purification of palmitoylated PSD-95

To purify full-length palmitoylated PSD-95 as the antigen, PSD-95-GFP was fused to a PSTCD tag (see Plasmid constructions), which undergoes biotinylation by endogenous enzymes in mammalian cells (Lorenzon et al., 2004). PSD-95-GFP-TEV-PSTCD and DHHC15, which stoichiometrically palmitoylate PSD-95 (Fukata et al., 2004), were coexpressed in HEK293T cells for 24 h. The cells were then lysed with buffer A (25 mM Tris-HCl, pH 7.5, 2 mM EDTA, 100 mM NaCl, 2% Triton X-100, and 50 µg/ml PMSF). The lysates were spun at 20,000 *g* for 30 min at 4°C and the supernatants were mixed with streptavidin-coated magnetic beads (SA Dynabeads M-280; Invitrogen) for 2 h at 4°C. The beads were washed with buffer B (25 mM Tris-HCl, pH 7.5, 2 mM EDTA, 100 mM NaCl, 0.1% Triton X-100, and 1 mM DTT) and used for antibody phage display screening.

Antibody phage display screening

The screening was performed using the Griffin.1 library of scFv, which is a random combination of human repertories of heavy and light chains that was provided by G. Winter (MRC, Cambridge, England, UK; www.lifesciences.sourcebioscience.com; Nizak et al., 2003a,b; Dimitrov et al., 2008). In brief, phages bound to PSD-95-GFP-TEV-PSTCD immobilized onto SA beads were eluted together with PSD-95-GFP by incubation with TEV protease. After the third round of selection, analysis of individual clones was performed. 80 scFv-expressing clones were analyzed and used to stain HeLa cells transfected with PSD-95-GFP by immunofluorescence. 16 clones clearly co-labeling with PSD-95-GFP were sequenced. They were all identical to PF11, which was chosen as the representative clone. For improved immunofluorescence, the PF11 scFv was subcloned into a plasmid to express a fusion protein with dimeric IgG Fc domains of human origin (Moutel et al., 2009). scFv fused to human Fc was expressed and secreted as hPF11 antibody from CHO cells. To express PF11 as a fluorescent intrabody, the entire PF11 cDNA was fused with GFP or mCherry cDNA (see Plasmid constructions).

In vivo palmitate labeling

HEK293T cells transfected with PSD-95-GFP-PSTCD and HA-DHHC15 were preincubated for 30 min in serum-free DMEM with fatty acid–free bovine serum albumin (BSA, 5 mg/ml; Sigma-Aldrich). Cells were then labeled with 0.25 mCi/ml [^{3}H]palmitic acid for 4 h in the preincubation medium. Cells were washed with PBS and scraped with SDS-PAGE sample buffer in the presence of 10 mM DTT. The cell lysate was resolved by SDS-PAGE, followed by fluorography (36-h exposure) and Western blotting. Transferred membranes were also analyzed by Coomassie brilliant blue staining.

Neuronal cell culture and immunofluorescence analysis

All animal studies described herein were reviewed and approved by the ethics committee at our institutions and all animals were handled according to the institutional guidelines concerning the care and handling of experimental animals. Rat hippocampal neurons (5 × 10^4 cells) were seeded onto poly-L-lysine–coated 12-mm coverslips in 24-well dishes and cultured in neurobasal medium (Invitrogen) supplemented with B-27 and 2 mM glutamax. Neurons were fixed with methanol for 10 min at −30°C (for hPF11 and DHHC2) or with 4% paraformaldehyde for 10 min at room temperature (for other antibodies), and blocked with PBS containing 10 mg/ml BSA for 10 min on ice. For hPF11, PSD-95, DHHC2, or vGlut1/vGlut2 staining, neurons were visualized with anti–human IgG Fc, anti–mouse IgG, anti–mouse IgG_1, or anti–guinea pig IgG secondary antibody, respectively. For 2C-STED imaging, ATTO425-conjugated anti–mouse or anti–rabbit IgG (Rockland, Inc.) and DyLight488-conjugated anti–human IgG Fc (Jackson ImmunoResearch Laboratories) or Chromeo 505–conjugated anti–mouse IgG (Active Motif) were used as the secondary antibodies. Specimens were mounted in ProLong Gold (Invitrogen). For knockdown or molecular replacement experiments, neurons (12 DIV) were transfected with the indicated knockdown vectors by Lipofectamine 2000 for 6 d, followed by immunofluorescence. To see surface expression of DHHCs-$_{lum}$HA in neurons, cells were transfected at 8 DIV and stained at 18 DIV. DHHCs-$_{lum}$HA were "live" labeled with an antibody to an extracellular HA-epitope (rat, 3F10) by incubating neurons in conditioned medium for 15 min at 37°C. Neurons were then fixed in 2% paraformaldehyde for 20 min and blocked. Surface DHHCs-$_{lum}$HA was visualized with an Alexa Fluor 488–conjugated secondary antibody. Neurons were subsequently permeabilized with 0.1% Triton X-100 for 10 min, and blocked. Total DHHCs-$_{lum}$HA was stained by anti-HA antibody (mouse, 16B12) and Cy3-conjugated secondary antibody. For acute synaptic activation of neurons, neurons (18–21 DIV) were briefly washed with buffer C (119 mM NaCl, 5 mM KCl, 2 mM $CaCl_2$, 2 mM $MgCl_2$, 33 mM D-glucose, 0.5 µM TTX, and 25 mM Hepes, pH 7.4). Then, neurons were stimulated with buffer D containing 90 mM KCl (34 mM NaCl, 90 mM KCl, 2 mM $CaCl_2$, 2 mM $MgCl_2$, 33 mM D-glucose, 0.5 µM TTX, 0.1 mM picrotoxin, and 25 mM Hepes, pH 7.4) for 5 min at 37°C (Carroll et al., 1999; Pickard et al., 2001). After washing with buffer C thoroughly, neurons were further incubated with buffer C for 1 h, followed by immunofluorescence analysis. For 2C-STED imaging of surface AMPARs (Fig. 9 A), after treatment of neurons with 90 mM KCl, neurons were thoroughly washed by buffer C and surface GluA1 was "live" labeled with an antibody to an extracellular epitope of GluA1 in buffer C by incubating neurons for 10 min at 37°C. Neurons were then fixed with methanol for 10 min at −30°C and stained by ATTO425-conjugated anti–rabbit antibody, followed by hPF11 staining with DyLight488-conjugated anti–human IgG Fc.

Fluorescent images were acquired with a confocal laser scanning microscopy system (LSM5 Exciter; Carl Zeiss) using a Plan Apochromat 63×/1.40 NA oil immersion objective lens. Microscope control and image analysis were performed using ZEN software (Carl Zeiss). For 2C-STED analysis, neurons were imaged with a confocal system (TCS SP5II STED CW; Leica) using an HCX PL APO 100×/1.40 NA oil immersion objective lens, combined with the Leica HyD detectors. Depletion was accomplished with a STED laser at 592 nm. ATTO425 and DyLight488 or Chromeo 505 were excited at 458 and 514 nm, respectively. Obtained confocal and STED images were further deconvoluted with the built-in deconvolution algorithms of the LAS-AF software (Leica). To measure the size of hPF11-stained postsynaptic membrane regions (Fig. 4 G), intensity profiles were drawn across the longest dimension of the hPF11-stained regions (nanodomains were not discriminated, see Fig. S2 B), and the full width at half maximum (FWHM) was determined using LAS-AF software (Leica). Gaussian approximation was performed by IGOR Pro software (WaveMetrics). Intensity profiles in two channels for hPF11 and PSD-95 labeling were used for measurement of distance of both signals (Fig. S5 A). In Fig. 8 (A and B), the mean intensity of PF11 signals overlapped with PSD-95 signals was measured with confocal microscopy. In Fig. 9 (A and B), the maximum intensity of all PF11 signals and overlapping surface GluA1 signals was measured with STED microscopy. Brightness and contrast adjustments were applied to the whole image using Photoshop CS4 (Adobe).

The reason why the intensity of total PSD-95 in dendritic spines was reduced by the treatment with 2-BP or KCl (Fig. 2 C and Fig. 8 A) may be that cytosolic PSD-95, which is depalmitoylated and diffused into the cytoplasm of the dendritic spines and shafts, is not efficiently detected by the conventional fluorescence microscopy, as compared with clustered PSD-95.

Live imaging

HEK293T cells were seeded onto poly-D-lysine–coated 35-mm glass-bottom dishes (2.5 × 10^5 cells/well; Iwaki). At 16 h after transfection with the indicated plasmids, cells were observed with a confocal laser microscopy system equipped with a Plan Apochromat 63×/1.40 NA oil immersion objective lens (LSM5 Exciter; Carl Zeiss) at 37°C in a 5% CO_2 culture chamber (Tokai Hit). Neurons were transfected with 2 µg of total DNA (PF11-GFP, PF11-Venus, or PSD-95-GFP together with indicated vectors) by the Amaxa nucleofector (Lonza) before seeding. Time-lapse imaging (Fig. 3, G and H)

was performed at 17–21 DIV with the same equipment. 3D image stacks were taken on dendritic regions of a neuron and then projected to 2D images using maximal intensity.

For RUSH analysis (Boncompain et al., 2012), HEK293T cells were cotransfected with a RUSH plasmid containing ER-hook (streptavidin-li) and SBP-GFP-DHHC2 together with pGW1-PSD-95-mCherry. At time 0, 40 µM D-biotin and 25 µM anisomycin were added and xyzt scans were performed every 1 min for 90 min with a laser-based auto-focusing system (adaptive focus control) at 37°C in a 5% CO_2 culture chamber with the confocal mode of a confocal system (TCS SP5 II; Leica) with the HyD detectors. Objective lens used was an HCX PL APO 63×/1.40 NA oil. Kymographs were produced using MetaMorph software version 7.7 (Molecular Devices).

For FRAP analysis, neurons were transfected with PF11-GFP or PSD-95-GFP, and the dendritic region indicated by a white rectangle was bleached with a 488-nm laser. We acquired xyz stacks at a spacing of 0.5 µm (5–7 sections) every 2 min for 1 h, with or without 2-BP treatment at 37°C in a 5% CO_2 culture chamber with the confocal mode of a Leica TCS SP5 II with the HyD detectors. Images were reconstructed using maximum intensity projections; individual clusters in the spine were tracked at each frame, and their average intensities were plotted in the graph. To exclude the effect of rapid diffusion of GFP probes from soma to the dendrite (shaft and spine), background fluorescence intensities in the bleached dendritic shaft were subtracted from those in the individual cluster at every time point. Image analysis was performed with LAS-AF software (Leica). Our FRAP data fit with the data of rapid palmitate turnover on PSD-95 measured by the pulse-chase method (El-Husseini Ael et al., 2002), but does not with the data of slow turnover measured by the acyl-biotinyl exchange method (Thomas et al., 2012). Although these biochemical methods showed different extents of palmitate turnover on PSD-95 (El-Husseini Ael et al., 2002; Kang et al., 2008; Noritake et al., 2009; Thomas et al., 2012), our FRAP analysis with PF11-GFP could allow us to sensitively detect rapid palmitate turnover on PSD-95 at the level of individual spines.

For live STED imaging of PF11-GFP or PSD-95-GFP, neurons transfected as above were observed at 23°C in a 5% CO_2 culture chamber. To directly compare STED with confocal imaging, the same optical fields were acquired in both modes by turning the STED laser on or off. For the measurement of the size of nanodomains (Fig. 4, C and D), we determined FWHM of line profiles of pixel intensity across the longest axis of randomly selected subsynaptic clusters using LAS-AF software (Leica).

To examine the relationship between PF11-Venus nanodomains and surface GluA1 (Fig. 4 H), surface GluA1 was "live" labeled with an antibody to an extracellular epitope of GluA1 by incubating neurons for 15 min at 37°C. After washing with neurobasal medium, neurons were labeled by an ATTO425-conjugated secondary antibody for 15 min. After neurons were washed with buffer C, living neurons were quickly observed at 458 and 514 nm excitation at room temperature by the STED mode.

Immunohistochemistry

An adult mouse brain was freshly frozen and embedded in the OCT compound. Then, the frozen sections (7 µm in thickness) were cut on a cryostat (CM1950; Leica) and fixed with acetone for 20 min on ice (paraformaldehyde fixation did not work for hPF11). Fixed sections were rehydrated and blocked for 1 h at room temperature in PBS containing 10% donkey and goat serum, and were incubated in the mixture of hPF11, PSD-95, and vGlut antibodies overnight at 4°C, followed by DyLight488 anti–human IgG Fc, Cy3 anti–mouse IgG, and Alexa Fluor 648 anti–guinea pig IgG secondary antibodies, respectively. Fluorescent images were acquired with a confocal laser scanning microscopy system (TCS SP5 II; Leica) equipped with an HCX PL APO 63×/1.40 oil immersion objective lens. To examine whether treatment with NH_2OH (which removes palmitate from PSD-95) abolishes staining by hPF11, we treated fixed brain sections or cultured neurons with NH_2OH. But the staining with hPF11 antibody was not affected (not depicted). Given that PF11 recognizes the conformation of palmitoylated PSD-95, it may be reasonably explained because PSD-95 conformation does not change after the fixation even if palmitate is removed from PSD-95 by NH_2OH.

Immunoprecipitation

HEK293T cells or hippocampal neurons transfected with PF11-GFP were lysed in 1 ml of buffer E (50 mM Tris-HCl, pH 8.0, 150 mM NaCl, 1% Igepal CA-630, 0.5% deoxycholate, and 0.1% SDS). After extraction for 20 min and centrifugation at 20,000 *g* for 5 min, the samples were incubated with rabbit anti-GFP antibody for 1 h at 4°C. Protein A–Sepharose (GE Healthcare) was added and incubated for 1 h at 4°C. Immunoprecipitates were washed three times with buffer F (20 mM Tris-HCl, pH 7.4, 1 mM EDTA, 100 mM NaCl, and 1% Triton X-100). Immunoprecipitates were resolved by SDS-PAGE, followed by Western blotting with anti-GFP and anti-mCherry (for HEK293T cells) or anti–PSD-95 (for neurons) antibodies.

Engagement of DHHC2-$_{lum}$HA on the cell surface

COS7 cells were transfected with DHHC2-$_{lum}$HA and the indicated plasmids. After transfection, cells were placed on ice for 15 min and then incubated with anti-HA antibody (3F10) for 1 h on ice. After washing with ice-cold DMEM, cells were treated with Cy3-conjugated anti–rat antibody for 1 h at 4°C without fixation. Subsequently, the cells were washed and transferred to 37°C for 1 h with or without 2-BP to induce immobile DHHC2-$_{lum}$HA clusters at the cell surface. Then the cells were fixed with 4% formaldehyde and examined for PSD-95-GFP recruitment in COS7 cells. Similar experiments were conducted using transfected hippocampal neurons, which were examined by subsequent immunofluorescence analysis to see whether engagements of DHHC2-$_{lum}$HA on the cell surface recruit endogenous palmitoylated PSD-95 (hPF11).

Statistical analysis

For paired sample comparisons, Student's *t* tests were used. For multiple test subjects, one-way ANOVA with post-hoc Tukey's tests were used. Error bars denote the standard deviation (SD). Box-and-whisker plots are shown to identify the median, 25th, and 75th percentiles, as well as the extremes.

Online supplemental materials

Fig. S1 shows that PF11 intrabody recognizes the conformation of palmitoylated PSD-95 and does not affect the PSD-95 function. Fig. S2 shows postsynaptic nanodomains visualized by PF11-GFP, PSD-95-GFP, and hPF11. Fig. S3 shows that palmitoylation, but not myristoylation, is necessary for the postsynaptic clustering of PSD-95. Fig. S4 shows the schematic diagram of RUSH and cell surface engagement assays. Fig. S5 shows that synaptic activation causes intra-spine delocalization of depalmitoylated PSD-95 and reduces the size of the postsynaptic membrane region. Video 1 shows that the FRAP of PSD-95-GFP is very slow. Video 2 shows that the FRAP of PF11-GFP is much faster. Video 3 shows that acutely induced plasma membrane insertion of DHHC2 triggers accumulation of PSD-95 at the plasma membrane. Video 4 shows that the treatment with 2-BP blocks DHHC2-induced PSD-95 accumulation at the plasma membrane. Video 5 shows that catalytically inactive DHHC2 (CS) does not accumulate PSD-95 at the plasma membrane. Online supplemental material is available at http://www.jcb.org/cgi/content/full/jcb.201302071/DC1.

We thank J. Noritake for cell surface engagement analysis, T. Iwanaga for technical support, N. Yokoi for Gaussian approximation analysis, and M. Matsuda (Kyoto University, Kyoto, Japan) for kind help. The authors are also indebted to S. Moutel for her help in setting up the antibody phage display system.

M. Fukata and F. Perez were supported by grants from the Human Frontier Science Program (HFSP, RGY0059-06). Y. Fukata is supported by grants from the HFSP (CDA0015-07) and the Ministry of Education, Culture, Sports, Science, and Technology (MEXT, 23110520). A. Dimitrov is supported by grants from Association Française contre les Myopathies and the HFSP (LT000029/2010-L). F. Perez is supported by the Centre National de la Recherche Scientifique (CNRS), by the Institut Curie, and by grants from the Agence Nationale de la Recherche (ANR-09-BLAN-0290) and the Institut National du Cancer (2009-1-PL BIO-12-IC-1). M. Fuakta is supported by the Funding Program for Next Generation World-Leading Researchers (LS123). Y. Fuakta and M. Fukata greatly appreciate support and encouragement from the PRESTO programs of JST.

Submitted: 14 February 2013
Accepted: 3 June 2013

References

Arellano, J.I., R. Benavides-Piccione, J. Defelipe, and R. Yuste. 2007. Ultrastructure of dendritic spines: correlation between synaptic and spine morphologies. *Front Neurosci*. 1:131–143. http://dx.doi.org/10.3389/neuro.01.1.1.010.2007

Béïque, J.C., D.T. Lin, M.G. Kang, H. Aizawa, K. Takamiya, and R.L. Huganir. 2006. Synapse-specific regulation of AMPA receptor function by PSD-95. *Proc. Natl. Acad. Sci. USA*. 103:19535–19540. http://dx.doi.org/10.1073/pnas.0608492103

Blanpied, T.A., J.M. Kerr, and M.D. Ehlers. 2008. Structural plasticity with preserved topology in the postsynaptic protein network. *Proc. Natl. Acad. Sci. USA*. 105:12587–12592. http://dx.doi.org/10.1073/pnas.0711669105

Boncompain, G., S. Divoux, N. Gareil, H. de Forges, A. Lescure, L. Latreche, V. Mercanti, F. Jollivet, G. Raposo, and F. Perez. 2012. Synchronization of

secretory protein traffic in populations of cells. *Nat. Methods*. 9:493–498. http://dx.doi.org/10.1038/nmeth.1928

Carroll, R.C., E.C. Beattie, H. Xia, C. Lüscher, Y. Altschuler, R.A. Nicoll, R.C. Malenka, and M. von Zastrow. 1999. Dynamin-dependent endocytosis of ionotropic glutamate receptors. *Proc. Natl. Acad. Sci. USA*. 96:14112–14117. http://dx.doi.org/10.1073/pnas.96.24.14112

Chen, X., C.D. Nelson, X. Li, C.A. Winters, R. Azzam, A.A. Sousa, R.D. Leapman, H. Gainer, M. Sheng, and T.S. Reese. 2011. PSD-95 is required to sustain the molecular organization of the postsynaptic density. *J. Neurosci.* 31:6329–6338. http://dx.doi.org/10.1523/JNEUROSCI.5968-10.2011

Chih, B., H. Engelman, and P. Scheiffele. 2005. Control of excitatory and inhibitory synapse formation by neuroligins. *Science*. 307:1324–1328. http://dx.doi.org/10.1126/science.1107470

Chisari, M., D.K. Saini, V. Kalyanaraman, and N. Gautam. 2007. Shuttling of G protein subunits between the plasma membrane and intracellular membranes. *J. Biol. Chem.* 282:24092–24098. http://dx.doi.org/10.1074/jbc.M704246200

Craven, S.E., A.E. El-Husseini, and D.S. Bredt. 1999. Synaptic targeting of the postsynaptic density protein PSD-95 mediated by lipid and protein motifs. *Neuron*. 22:497–509. http://dx.doi.org/10.1016/S0896-6273(00)80705-9

Dani, A., B. Huang, J. Bergan, C. Dulac, and X. Zhuang. 2010. Superresolution imaging of chemical synapses in the brain. *Neuron*. 68:843–856. http://dx.doi.org/10.1016/j.neuron.2010.11.021

Dimitrov, A., M. Quesnoit, S. Moutel, I. Cantaloube, C. Poüs, and F. Perez. 2008. Detection of GTP-tubulin conformation in vivo reveals a role for GTP remnants in microtubule rescues. *Science*. 322:1353–1356. http://dx.doi.org/10.1126/science.1165401

Ehrlich, I., M. Klein, S. Rumpel, and R. Malinow. 2007. PSD-95 is required for activity-driven synapse stabilization. *Proc. Natl. Acad. Sci. USA*. 104:4176–4181. http://dx.doi.org/10.1073/pnas.0609307104

El-Husseini Ael, D., and D.S. Bredt. 2002. Protein palmitoylation: a regulator of neuronal development and function. *Nat. Rev. Neurosci.* 3:791–802. http://dx.doi.org/10.1038/nrn940

El-Husseini, A.E., S.E. Craven, D.M. Chetkovich, B.L. Firestein, E. Schnell, C. Aoki, and D.S. Bredt. 2000a. Dual palmitoylation of PSD-95 mediates its vesiculotubular sorting, postsynaptic targeting, and ion channel clustering. *J. Cell Biol.* 148:159–172. http://dx.doi.org/10.1083/jcb.148.1.159

El-Husseini, A.E., E. Schnell, D.M. Chetkovich, R.A. Nicoll, and D.S. Bredt. 2000b. PSD-95 involvement in maturation of excitatory synapses. *Science*. 290:1364–1368.

El-Husseini Ael, D., E. Schnell, S. Dakoji, N. Sweeney, Q. Zhou, O. Prange, C. Gauthier-Campbell, A. Aguilera-Moreno, R.A. Nicoll, and D.S. Bredt. 2002. Synaptic strength regulated by palmitate cycling on PSD-95. *Cell*. 108:849–863. http://dx.doi.org/10.1016/S0092-8674(02)00683-9

Elias, G.M., and R.A. Nicoll. 2007. Synaptic trafficking of glutamate receptors by MAGUK scaffolding proteins. *Trends Cell Biol.* 17:343–352. http://dx.doi.org/10.1016/j.tcb.2007.07.005

Elias, G.M., L. Funke, V. Stein, S.G. Grant, D.S. Bredt, and R.A. Nicoll. 2006. Synapse-specific and developmentally regulated targeting of AMPA receptors by a family of MAGUK scaffolding proteins. *Neuron*. 52:307–320. http://dx.doi.org/10.1016/j.neuron.2006.09.012

Fukata, Y., and M. Fukata. 2010. Protein palmitoylation in neuronal development and synaptic plasticity. *Nat. Rev. Neurosci.* 11:161–175. http://dx.doi.org/10.1038/nrn2788

Fukata, M., Y. Fukata, H. Adesnik, R.A. Nicoll, and D.S. Bredt. 2004. Identification of PSD-95 palmitoylating enzymes. *Neuron*. 44:987–996. http://dx.doi.org/10.1016/j.neuron.2004.12.005

Funke, L., S. Dakoji, and D.S. Bredt. 2005. Membrane-associated guanylate kinases regulate adhesion and plasticity at cell junctions. *Annu. Rev. Biochem.* 74:219–245. http://dx.doi.org/10.1146/annurev.biochem.74.082803.133339

Gorleku, O.A., A.M. Barns, G.R. Prescott, J. Greaves, and L.H. Chamberlain. 2011. Endoplasmic reticulum localization of DHHC palmitoyltransferases mediated by lysine-based sorting signals. *J. Biol. Chem.* 286:39573–39584. http://dx.doi.org/10.1074/jbc.M111.272369

Graf, E.R., X. Zhang, S.X. Jin, M.W. Linhoff, and A.M. Craig. 2004. Neurexins induce differentiation of GABA and glutamate postsynaptic specializations via neuroligins. *Cell*. 119:1013–1026. http://dx.doi.org/10.1016/j.cell.2004.11.035

Greaves, J., J.A. Carmichael, and L.H. Chamberlain. 2011. The palmitoyl transferase DHHC2 targets a dynamic membrane cycling pathway: regulation by a C-terminal domain. *Mol. Biol. Cell*. 22:1887–1895. http://dx.doi.org/10.1091/mbc.E10-11-0924

Hayashi, M.K., C. Tang, C. Verpelli, R. Narayanan, M.H. Stearns, R.M. Xu, H. Li, C. Sala, and Y. Hayashi. 2009. The postsynaptic density proteins Homer and Shank form a polymeric network structure. *Cell*. 137:159–171. http://dx.doi.org/10.1016/j.cell.2009.01.050

Kang, R., R. Swayze, M.F. Lise, K. Gerrow, A. Mullard, W.G. Honer, and A. El-Husseini. 2004. Presynaptic trafficking of synaptotagmin I is regulated by protein palmitoylation. *J. Biol. Chem.* 279:50524–50536. http://dx.doi.org/10.1074/jbc.M404981200

Kang, R., J. Wan, P. Arstikaitis, H. Takahashi, K. Huang, A.O. Bailey, J.X. Thompson, A.F. Roth, R.C. Drisdel, R. Mastro, et al. 2008. Neural palmitoyl-proteomics reveals dynamic synaptic palmitoylation. *Nature*. 456:904–909. http://dx.doi.org/10.1038/nature07605

Kim, E., and M. Sheng. 2004. PDZ domain proteins of synapses. *Nat. Rev. Neurosci.* 5:771–781. http://dx.doi.org/10.1038/nrn1517

Kuriu, T., A. Inoue, H. Bito, K. Sobue, and S. Okabe. 2006. Differential control of postsynaptic density scaffolds via actin-dependent and -independent mechanisms. *J. Neurosci.* 26:7693–7706. http://dx.doi.org/10.1523/JNEUROSCI.0522-06.2006

Linder, M.E., and R.J. Deschenes. 2007. Palmitoylation: policing protein stability and traffic. *Nat. Rev. Mol. Cell Biol.* 8:74–84. http://dx.doi.org/10.1038/nrm2084

Lorenzon, N.M., C.S. Haarmann, E.E. Norris, S. Papadopoulos, and K.G. Beam. 2004. Metabolic biotinylation as a probe of supramolecular structure of the triad junction in skeletal muscle. *J. Biol. Chem.* 279:44057–44064. http://dx.doi.org/10.1074/jbc.M405318200

McCormick, C.J., S. Maucourant, S. Griffin, D.J. Rowlands, and M. Harris. 2006. Tagging of NS5A expressed from a functional hepatitis C virus replicon. *J. Gen. Virol.* 87:635–640. http://dx.doi.org/10.1099/vir.0.81553-0

Miesenböck, G., D.A. De Angelis, and J.E. Rothman. 1998. Visualizing secretion and synaptic transmission with pH-sensitive green fluorescent proteins. *Nature*. 394:192–195. http://dx.doi.org/10.1038/28190

Moutel, S., A. El Marjou, O. Vielemeyer, C. Nizak, P. Benaroch, S. Dübel, and F. Perez. 2009. A multi-Fc-species system for recombinant antibody production. *BMC Biotechnol.* 9:14. http://dx.doi.org/10.1186/1472-6750-9-14

Nakagawa, T., K. Futai, H.A. Lashuel, I. Lo, K. Okamoto, T. Walz, Y. Hayashi, and M. Sheng. 2004. Quaternary structure, protein dynamics, and synaptic function of SAP97 controlled by L27 domain interactions. *Neuron*. 44:453–467. http://dx.doi.org/10.1016/j.neuron.2004.10.012

Nam, C.I., and L. Chen. 2005. Postsynaptic assembly induced by neurexin-neuroligin interaction and neurotransmitter. *Proc. Natl. Acad. Sci. USA*. 102:6137–6142. http://dx.doi.org/10.1073/pnas.0502038102

Nizak, C., S. Martin-Lluesma, S. Moutel, A. Roux, T.E. Kreis, B. Goud, and F. Perez. 2003a. Recombinant antibodies against subcellular fractions used to track endogenous Golgi protein dynamics in vivo. *Traffic*. 4:739–753. http://dx.doi.org/10.1034/j.1600-0854.2003.00132.x

Nizak, C., S. Monier, E. del Nery, S. Moutel, B. Goud, and F. Perez. 2003b. Recombinant antibodies to the small GTPase Rab6 as conformation sensors. *Science*. 300:984–987. http://dx.doi.org/10.1126/science.1083911

Noritake, J., Y. Fukata, T. Iwanaga, N. Hosomi, R. Tsutsumi, N. Matsuda, H. Tani, H. Iwanari, Y. Mochizuki, T. Kodama, et al. 2009. Mobile DHHC palmitoylating enzyme mediates activity-sensitive synaptic targeting of PSD-95. *J. Cell Biol.* 186:147–160. http://dx.doi.org/10.1083/jcb.200903101

Petersen, J.D., X. Chen, L. Vinade, A. Dosemeci, J.E. Lisman, and T.S. Reese. 2003. Distribution of postsynaptic density (PSD)-95 and Ca2+/calmodulin-dependent protein kinase II at the PSD. *J. Neurosci.* 23:11270–11278.

Pickard, L., J. Noël, J.K. Duckworth, S.M. Fitzjohn, J.M. Henley, G.L. Collingridge, and E. Molnar. 2001. Transient synaptic activation of NMDA receptors leads to the insertion of native AMPA receptors at hippocampal neuronal plasma membranes. *Neuropharmacology*. 41:700–713. http://dx.doi.org/10.1016/S0028-3908(01)00127-7

Rao, A., E. Kim, M. Sheng, and A.M. Craig. 1998. Heterogeneity in the molecular composition of excitatory postsynaptic sites during development of hippocampal neurons in culture. *J. Neurosci.* 18:1217–1229.

Resh, M.D. 2006. Palmitoylation of ligands, receptors, and intracellular signaling molecules. *Sci. STKE*. 2006:re14. http://dx.doi.org/10.1126/stke.3592006re14

Rocks, O., A. Peyker, M. Kahms, P.J. Verveer, C. Koerner, M. Lumbierres, J. Kuhlmann, H. Waldmann, A. Wittinghofer, and P.I. Bastiaens. 2005. An acylation cycle regulates localization and activity of palmitoylated Ras isoforms. *Science*. 307:1746–1752. http://dx.doi.org/10.1126/science.1105654

Salaun, C., J. Greaves, and L.H. Chamberlain. 2010. The intracellular dynamic of protein palmitoylation. *J. Cell Biol.* 191:1229–1238. http://dx.doi.org/10.1083/jcb.201008160

Sen, N., and S.H. Snyder. 2010. Protein modifications involved in neurotransmitter and gasotransmitter signaling. *Trends Neurosci.* 33:493–502. http://dx.doi.org/10.1016/j.tins.2010.07.004

Shaner, N.C., P.A. Steinbach, and R.Y. Tsien. 2005. A guide to choosing fluorescent proteins. *Nat. Methods*. 2:905–909. http://dx.doi.org/10.1038/nmeth819

Subach, F.V., G.H. Patterson, S. Manley, J.M. Gillette, J. Lippincott-Schwartz, and V.V. Verkhusha. 2009. Photoactivatable mCherry for high-resolution two-color fluorescence microscopy. *Nat. Methods*. 6:153–159. http://dx.doi.org/10.1038/nmeth.1298

Sumioka, A., D. Yan, and S. Tomita. 2010. TARP phosphorylation regulates synaptic AMPA receptors through lipid bilayers. *Neuron*. 66:755–767. http://dx.doi.org/10.1016/j.neuron.2010.04.035

Swulius, M.T., Y. Kubota, A. Forest, and M.N. Waxham. 2010. Structure and composition of the postsynaptic density during development. *J. Comp. Neurol.* 518:4243–4260. http://dx.doi.org/10.1002/cne.22451

Thomas, G.M., T. Hayashi, S.L. Chiu, C.M. Chen, and R.L. Huganir. 2012. Palmitoylation by DHHC5/8 targets GRIP1 to dendritic endosomes to regulate AMPA-R trafficking. *Neuron*. 73:482–496. http://dx.doi.org/10.1016/j.neuron.2011.11.021

Tomita, S., L. Chen, Y. Kawasaki, R.S. Petralia, R.J. Wenthold, R.A. Nicoll, and D.S. Bredt. 2003. Functional studies and distribution define a family of transmembrane AMPA receptor regulatory proteins. *J. Cell Biol.* 161:805–816. http://dx.doi.org/10.1083/jcb.200212116

Tomita, S., M. Fukata, R.A. Nicoll, and D.S. Bredt. 2004. Dynamic interaction of stargazin-like TARPs with cycling AMPA receptors at synapses. *Science*. 303:1508–1511. http://dx.doi.org/10.1126/science.1090262

Topinka, J.R., and D.S. Bredt. 1998. N-terminal palmitoylation of PSD-95 regulates association with cell membranes and interaction with K+ channel Kv1.4. *Neuron*. 20:125–134. http://dx.doi.org/10.1016/S0896-6273(00)80440-7

Tsutsumi, R., Y. Fukata, J. Noritake, T. Iwanaga, F. Perez, and M. Fukata. 2009. Identification of G protein alpha subunit-palmitoylating enzyme. *Mol. Cell. Biol.* 29:435–447. http://dx.doi.org/10.1128/MCB.01144-08

Valtschanoff, J.G., and R.J. Weinberg. 2001. Laminar organization of the NMDA receptor complex within the postsynaptic density. *J. Neurosci.* 21:1211–1217.

Varoqueaux, F., G. Aramuni, R.L. Rawson, R. Mohrmann, M. Missler, K. Gottmann, W. Zhang, T.C. Südhof, and N. Brose. 2006. Neuroligins determine synapse maturation and function. *Neuron*. 51:741–754. http://dx.doi.org/10.1016/j.neuron.2006.09.003

Vielemeyer, O., C. Nizak, A.J. Jimenez, A. Echard, B. Goud, J. Camonis, J.C. Rain, and F. Perez. 2010. Characterization of single chain antibody targets through yeast two hybrid. *BMC Biotechnol.* 10:59. http://dx.doi.org/10.1186/1472-6750-10-59